Monthly Notices of the ROYAL ASTRONOMICAL SOCIETY

MNRAS **501,** 3750–3766 (2021) doi:10.1093/mnras/staa3850

The physical properties and evolution of the interacting system AM 1204−292

D. A. Rosa,[1]★ I. Rodrigues [1], A. C. Krabbe [1], A. C. Milone [2] and S. Carvalho[1]

[1]*Instituto de Pesquisa & Desenvolvimento (IP&D), Universidade do Vale do Paraíba, Av. Shishima Hifumi 2911, 12244-000 São José dos Campos–SP, Brazil*
[2]*Instituto Nacional de Pesquisas Espaciais (INPE), Divisão de Astrofísica, Av. dos Astronautas 1758, 12227-010 São José dos Campos–SP, Brazil*

Accepted 2020 December 7. Received 2020 December 6; in original form 2019 December 9

ABSTRACT

We investigate interaction effects in the stellar and gas kinematics, stellar population, and ionized gas properties of the interacting galaxy pair AM 1204−292,composed of NGC 4105 and NGC 4106. The data consist of long-slit spectra in the range 3000–7050 Å. The massive E3 galaxy NGC 4105 presents a flat stellar velocity profile, while the ionized gas is in strong rotation, suggesting an external origin. Its companion, NGC 4106, shows asymmetries in the radial velocity field, likely due to the interaction. The dynamics of the interacting pair were modelled using the P-Gadget3 TREEPM/SPH code, from which we show that the system has just passed the first perigalacticum, which triggered an outbreak of star formation, currently at full maximum. We characterized the stellar population properties using the stellar population synthesis code STARLIGHT and, on average, both galaxies are predominantly composed of old stellar populations. NGC 4105 has a slightly negative age gradient, comparable with that of the most massive elliptical galaxies, but a steeper metallicity gradient. The SB0 galaxy NGC 4106 presents smaller radial variations in both age and metallicity in comparison with intermediate-mass early-type galaxies. These gradients have not been disturbed by interaction, since the star formation happened very recently and was not extensive in mass. Electron density estimates for the pair are systematically higher than those obtained in isolated galaxies. The central O/H abundances were obtained from photoionization models in combination with emission-line ratios, which resulted in $12 + \log(\mathrm{O/H}) = 9.03 \pm 0.02$ and $12 + \log(\mathrm{O/H}) = 8.69 \pm 0.05$ for NGC 4105 and NGC 4106, respectively.

Key words: galaxies: abundances – galaxies: formation – galaxies: groups: general – galaxies: kinematics and dynamics – galaxies: stellar content.

1 INTRODUCTION

Interacting pairs of galaxies are excellent laboratories in which to study different aspects of galaxy evolution, such as morphological transformation, induced star formation, and fuelling of the central supermassive black hole (lighting an active nucleus: e.g. Fernandes de Mello 1995; De Mello et al. 1995, 1996; Longhetti et al. 2000; Focardi, Zitelli & Marinoni 2008; Rogers et al. 2009). Also, the study of binary galaxies at different interaction stages can provide important constraints on the hierarchical scenario of galaxy formation and evolution. The relatively small velocities of a close encounter in a gravitationally coupled pair of galaxies of comparable mass/size make the mutual interaction strong enough inside each galaxy to modify the structure of the galaxies. Numerous studies have reported that a close encounter between two galaxies modifies the mutual gravitational fields (Toomre & Toomre 1972). A close encounter can create new substructures in the gas, dust, and star spatial distributions, such as warps or bars, tidal tails, plumes, and bridges, pulled out by tidal forces during gravitational interaction (e.g. Mendes de Oliveira & Hickson 1994; Rodrigues et al. 1999; Barnes 2002; Renaud 2010; Presotto et al. 2010; Drzazga et al. 2011).

Mixed pairs of galaxies have components spanning different morphologies, such as an elliptical (early-type galaxy) and a spiral (late-type galaxy). This kind of galaxy pair becomes particularly interesting, because it represents a good site for investigating in detail those physical processes induced by close interactions (e.g. Fernandes de Mello 1995; De Mello et al. 1995, 1996). The Catalogue of Southern Peculiar Galaxies and Associations by Arp and Madore (Arp, Madore & Roberton 1987) became a pioneer compilation of galaxy pairs, in which a lot of mixed pairs can be found.

The dynamics of galaxy interactions can be studied through numerical simulations, including the stellar and gaseous components, besides dark matter, as primary ingredients. For instance, Moreno et al. (2015) embarked on a systematic study of 75 simulations of galaxies in major mergers. They reported that star formation is more elevated in the centre than on the outskirts of interacting galaxies, and concluded that these trends are most prominent in smaller companion galaxies with strongly aligned disc spin orientations. Another example is the numerical simulations by Torrey et al. (2012), which showed that the nuclear metallicity evolution is a perfect competition between metal-poor gas inflows and enrichment due to star formation (or feedback from star formation and active galactic nucleus (AGN) activity).

★ E-mail: deiserosa@univap.br

Mutual interaction between galaxies may enhance star formation (e.g. Larson & Tinsley 1978; Woods & Geller 2007; Krabbe et al. 2008; Patton et al. 2013; Knapen, Cisternas & Querejeta 2015). However, the environment might not play a determinant role in the formation and evolution of (very) massive early-type galaxies (e.g. Xu et al. 2010; Bait, Barway & Wadadekar 2017; Yadav & Chen 2018).

Star formation enhancements are accompanied by other events such as perturbations in the radial velocity field and dilution of the metallicity gradient. This is consistent with results obtained for chemical abundances and the mass–metallicity relation (Sánchez et al. 2013), which show that interaction-induced flows of low-metallicity gas from the outer parts of the disc of a galaxy can decrease the metallicity in the inner regions and modify the radial abundance gradients (e.g. Kewley et al. 2010; Rosa et al. 2014; Sánchez et al. 2014; Muñoz-Elgueta et al. 2018). We cannot exclude the possibility that the inflow of low-metallicity gas would be considered as the principal source that affects the nuclear metallicity of interacting galaxies. Although there is evidence for dilution in the central gas metallicity produced by interactions, a few interactions may also be able to enhance it (e.g. Barrera-Ballesteros et al. 2015), seen observationally by redder optical colours (e.g. Darg et al. 2010; Patton et al. 2011), for instance.

Strong interactions in close pairs may produce an inhomogeneity in the interstellar medium, shown as a wide variation in electron density (e.g. Krabbe et al. 2014; Roche et al. 2015). The formation of bars induced by perturbation from the companion is also observed (e.g. Méndez-Abreu et al. 2012; Alonso et al. 2018).

Active galactic nuclei can also be produced, fuelled by the infall of gas from the galaxy outskirts towards the central region, or even from a late-type galaxy to its companion (e.g. Eliche-Moral et al. 2011; Ellison et al. 2011; Satyapal et al. 2014; Donley et al. 2018). Gravitational interactions, as well as tidal effects, can provide fuel for a supermassive black hole in the centre of the galaxy (nucleus), leading to a connection between star formation and black hole activity (Trouille, Barger & Tremonti 2011; Silverman et al. 2011). The activity of the nucleus provides energy to the interstellar medium and can even smooth star formation (Croton et al. 2006; Di Matteo et al. 2008; Henriques et al. 2019). However, Weaver et al. (2018), who investigated the effects of galaxy mergers throughout the interaction sequence in NGC 7252 (nearest major-merger galaxy remnants), revealed the extent of ongoing star formation and the recent star formation history. Weaver et al. also found a large ionized gas cloud previously discovered ∼5 kpc south of the nucleus, which may be associated with a low-ionization nuclear emission-line region (LINER). Therefore, it is of great significance to study the properties of ionized gas in the circumnuclear region and AGNs connected with interacting galaxies in order to find evidence for the relationship between the active galactic nucleus and gravitational interaction.

This work presents a detailed study for the interacting system AM 1204−292, where the physical properties of the ionized gas, the characteristics of the stellar population, and the nuclear activity are linked with the process of interaction between galaxies and the destiny of this system is uncovered.

AM 1204−292 is a pair of galaxies with mixed morphology components, containing the very luminous elliptical galaxy NGC 4105 (according to the Third Reference Catalogue of Bright Galaxies: De Vaucouleurs et al. 1991, hereafter RC3), which however is classified as S0 in the Revised Shapley Ames Catalog of Bright Galaxies (Sandage & Tammann 1981, hereafter RSA), and NGC 4106, a (diffuse) lenticular barred galaxy with extended tidal arms produced by interaction (Koprolin & Zeilinger 2000). It was classified in RC3 as SB0(s)+ and in RSA as SB0/a (tides).

The galaxies are separated by a projected distance of 9.6 kpc and a difference in radial velocities of 274 km s^{-1}. There is visual evidence for one tidal arm in NGC 4106 that expands towards the primary galaxy in the south direction and its counterpart tidal arm/tail heading in the opposite direction. On the other side, NGC 4105 does not show clear signs of perturbation. The spectra of both galaxies are dominated by prominent absorption features (Donzelli & Pastoriza 2000) and some emission lines, such as [O II] λ3727 Å (Longhetti et al. 1998) and [N II] λ6584 Å (Caon, Macchetto & Pastoriza 2000). Moreover, Longhetti et al. (1998) found evidence from the line-strength indices that these galaxies experienced recent star formation episodes. Both galaxies are also fairly red, with $(B-V)$ colour index very similar to ∼+0.9 (Reduzzi & Rampazzo 1996). The X-ray luminosity of NGC 4105 is $L_x \sim 3.98 \times 10^{39}$ erg s^{-1} (0.5–2.0 keV) and that of NGC 4106 is $L_x \sim 1.26 \times 10^{39}$ erg s^{-1} (Grützbauch et al. 2007). Also, Grützbauch et al. (2009) found dusty features in the central region and modelled the brightness distribution, concluding that it presents a discy outer structure.

This work is organized as follows. In Section 2, we describe the observations and data reduction. The stellar and gas kinematics in each individual galaxy are presented in Section 3. The *N*-body + SPH simulations built to reproduce the interaction between the two galaxies and to uncover the destiny of this system are explored in Section 4. We present in Section 5 the procedure employed to perform stellar population synthesis and the respective results required to estimate the age distribution of the stellar populations. In Section 6, we analyse the results concerning the ionized gas properties, centring on electron density and oxygen abundance. Finally, we summarize our conclusions in Section 7.

2 OBSERVATIONS AND DATA REDUCTION

In Table 1, some general characteristics of the galaxy pair are listed, such as identification, morphology, absolute *B*-band magnitude, effective radius R_e (isophotal radius that contains half the total flux of the component), major axis direction (MA), and inclination angle (i) of each galaxy. The projected linear separation between the galaxy nuclei on the sky plane is about 9.6 kpc (adopting $H_0 = 73$ km s^{-1}Mpc^{-1} (Wright 2006) and the average distance of the galaxy pair of 28.6 Mpc).

The current study is based on long-slit spectroscopic observations carried out on 2017 March 4 with the Goodman High Throughput Spectrograph (GTHS) attached to the 4.10-m Southern Astrophysical Research (SOAR) telescope (Cerro Pachon, Chile). Spectra with the single long-slit mask were acquired in the range λλ3000–7050 Å with a grating of 400 line mm^{-1} (M1 mode) and a slit of 1.03-arcsec width, providing an average spectral resolution of 5.5 Å in the region λλ3800–6800 Å, a spectral sampling of 1 Å pixel^{-1}, and a spatial scale of 0.15 arcsec pixel^{-1}. The estimate of the spectral resolution was based on the broadening of He–Ar lines in the wavelength calibration spectra and cross-correlations between the stellar template spectra (representing $\sigma_{v,\,\mathrm{inst}} = 132$ km s^{-1}). The atmospheric seeing was about 1 arcsec and we also noted some cirrus clouds amongst the observations.

Long-slit spectra of the galaxy pair AM 1204−292 were taken at three different position angles (PA), in order to observe the central regions and the principal axes. PA=118° crosses the discs of NGC 4105, near the semi-major axis, and NGC 4106, but not in their centres. The minor photometric axis of the elliptical galaxy NGC 4105 was observed at PA = 46.4°. The slit at PA=161° crossed

Table 1. Main characteristics of the AM 1204−292 galaxy pair members: identification, morphology, total *B*-band luminosity, colour index ($B-V$), effective radius R_e, apparent major axis direction MA, and inclination angle *i*.

ID AM 1204−292	Morphology [1]	log L_B [6] ($L_\odot$)	$(B-V)$ [2] (mag)	R_e [3] (kpc)	MA [2, 4, 5] (°)	i [2, 5] (°)	Other designations
NGC 4105	E3	10.86	0.99	10.26	136.4	54.7	ESO440−054
NGC 4106	SB(s)0 +	10.75	1.01	3.47	91	50	ESO440−056

References: [1] De Vaucouleurs et al. (1991); [2] Hyperleda (Makarov et al. 2014); [3] Salo et al. (2015); [4] Capaccioli et al. (2015); [5] Herrera-Endoqui et al. (2015); [6] Trinchieri & Rampazzo (2001).

the centre of NGC 4106 and the southern tidal arm that extends toward NGC 4105.

Multiple spectra were taken at the same slit position to increase the signal-to-noise ratio and the exposure times were limited to 1200 s to minimize the effects of spurious cosmic rays. The slit positions are shown in Fig. 1, superimposed on the optical image of the pair. The journal of observations is listed in Table 2.

The spectroscopic data have been reduced with the IRAF[1] package. The standard spectroscopic reduction procedure has been applied: image trimming, bias subtraction, flat-field correction, sky background subtraction, cosmic-ray removal, one-dimensional spectrum extraction, and wavelength and flux calibrations. Each one-dimensional spectrum comprises the flux contained in an aperture of $1.03 \times 0.9\,\mathrm{arcsec}^2$, which at the distance to the pair corresponds to nearly 142×127.5 pc. The galactocentric radial coordinates to the positions of each aperture extracted from the slits were corrected, taking into account the inclination angles of each galaxy (given in Table 1), in order to make radial plots of the quantities of interest.

3 KINEMATICS

3.1 Stellar kinematics

The stellar radial velocity and line-of-sight velocity dispersion σ_v^* for each aperture were estimated from the cross-correlation of its absorption line spectrum against a set of stellar template spectra. The radial velocity was reduced to a heliocentric frame of reference cz_{Helio}, as usual. The rotation curve and the σ_v^* radial profile in the slit directions have been estimated for each galaxy to characterize the dynamical system.

We adopted the Radial Velocity Analysis package of Smithsonian Astrophysical Observatory (RVSAO: Kurtz & Mink 1998), from the IRAF package, to measure the radial velocity and velocity dispersion. Spectra of K giant stars (collected under the same instrumental setup as the galaxy pair observations) were used as reference for the cross-correlations, since optical spectra of evolved early-type galaxies (ETGs) are dominated by them. The observed K giants are HD 120452, HD 132345, and HD 136028. Their heliocentric radial velocities are from the Duflot et al. (1995) catalogue. The best stellar template from the cross-correlation of the nuclear aperture spectrum is assumed as a single template for all aperture spectra of each galaxy. The spectral range of cross-correlations is λλ3800 – 6800 Å and the Fourier filters are those suggested by Tonry & Davis (1979). A second-order polynomial function is employed to fit the half-height of the cross-correlation peak for estimating its full width at half-maximum (FWHM).

[1]Image Reduction and Analysis Facility, published by National Optical Astronomical Observatory (NOAO), operated by AURA, Inc, under agreement with NFS.

The observed radial velocity is simply read from the position of the correlation peak and its corresponding error is given directly by 3/8 (FWHM/(1 + *r*)), where *r* is the height of the correlation peak divided by the amplitude of a sinusoidal noise for the correlation function (Kurtz & Mink 1998). The velocity dispersion of each galaxy aperture spectrum has been estimated as a function of FWHM through a third-order polynomial fit. To establish the relation between σ_v and FWHM, we convoluted all three template spectra taken on March 4 using different Gaussians, representing σ_v from 50–500 km s^{-1} in steps of 50 km s^{-1}. Cross-correlations between the broadened template spectra and the respective observed stellar spectrum provide σ_v and FWHM. Errors in velocity dispersions were estimated by artificially adding Poisson noise to the broadened spectra of a stellar template.

The radial velocities after subtraction of the systemic velocities, the velocity dispersion σ_v^*, and the spatial profiles of the λ5735 continuum flux across the observed slit positions are shown in Fig. 2 (no geometric correction was applied, due to the inclination of the galaxy plane relative to the plane of the sky). These galaxies are separated by 1.15 arcmin in projection, corresponding to 9.6 kpc and a difference in radial velocities of ∼274 km s^{-1}. These values are very similar to those found by Kim et al. (2012).

3.1.1 *NGC 4105*

No signs of rotation were detected for the stellar component over both slit directions observed for this elliptical galaxy (see Fig. 2). For PA=46.4° we observe a U-shaped symmetry in the radial velocity, with values reaching 209 and 238 km s^{-1} at ∼3.36 (south-west, SW) and ∼3.24 kpc (north-east, NE), respectively, and no tendency to decline. In Section 4, we present the velocity map of a simulation that describes the dynamics of this pair quite well. We will then come back to this point. For PA=118°, the radial velocity and the velocity dispersion are approximately homogeneous along the radius, with a slight decline towards the south-east (SE) side, reaching a maximum value of 52 km s^{-1} at ∼1.5 kpc, probably due to interaction. We considered the heliocentric velocity of NGC 4105 as being a radial velocity measured at the continuum peak along the slit position at PA=46.4°, i.e. $v_r = 1949 \pm 18$ km s^{-1}.

Samurović & Danziger (2005) investigated dark matter in early-type galaxies through dynamical modelling and found that the velocities are not antisymmetric, due to interaction with the companion. These authors also found that the velocity dispersion decreases from central values of 320 – 200 km s^{-1}, in agreement with our results.

3.1.2 *NGC 4106*

This galaxy shows a nearly symmetrical rotation velocity curve across both slit directions. For the slit position crossing the nucleus, PA=161°, a heliocentric velocity of 2223 ± 15 km s^{-1} and a maximum value of the rotation velocity of ∼50 ± 21 km s^{-1} were

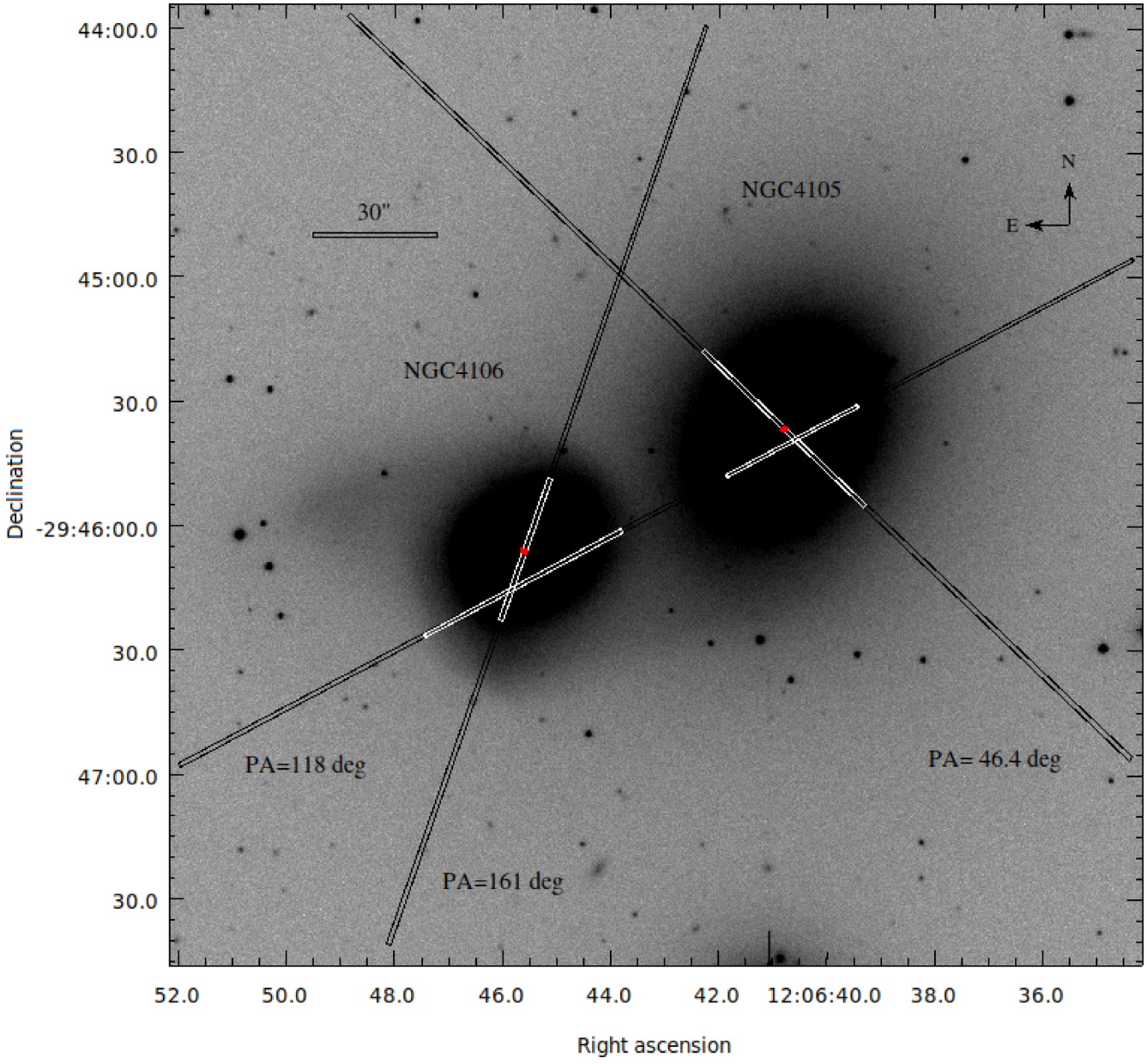

Figure 1. Slit positions for AM 1204−292 system superimposed on the optical image of the pair in the *I* band from the Carnegie–Irvine Galaxy Survey. The centre of each galaxy is marked in red.The white section of each slit shows the section of the slits from where useful data was extracted (Ho et al. 2011; Li et al. 2011).

Table 2. Galaxy ID, slit position, exposure time, and wavelength range of the spectra for the galaxy pair.

Galaxy ID	PA (°)	Exposure time (s)	Δλ (Å)
NGC 4105	46.4	3 × 1200	3000–7050
NGC 4106	161	3 × 1200	3000–7050
NGC 4105/06	118	2 × 1200	3000–7050

found. One side of the curve at ∼0.7 kpc towards the south-east of slit position PA=161° presents oscillations in the flat region of the curve of the order of 30 km s^{-1}, where the tidal arm originates. The most symmetrical, least-scattered, and smooth curve was derived using the slit position at PA=118°. Both sides of the curve display regions with fluctuations of about 20 km s^{-1}, one ∼0.5–1.5 kpc towards the north-west (NW) and another at ∼1–2 kpc towards the SE. The maximum rotation velocity is 128 ± 22 km s^{-1} at ∼1.82 kpc.

The radially symmetric velocity dispersion profiles obtained by us along both directions (PA=161° and PA=118°) are in good agreement with the results previously obtained by Longhetti et al. (1998).

Hence, we predict that the NGC 4106 galaxy shows a fairly significant rotational symmetry. For this reason, we adopted a very simple approximation for the observed velocity distribution: specifically, assuming circular orbits in a plane $P(i, \psi_0)$ characterized by the inclination relative to the plane of the sky (i) and the position angle (PA) of the line of nodes ψ_0. It results in an observed radial circular velocity at a position $v(R,\psi)$ in the plane of the sky given by (Bertola et al. 1991)

$$v(R, \psi) = V_s + \frac{V_0 R \cos(\psi - \psi_0) \sin(i) \cos(i)}{\sqrt{R^2[\sin^2(\psi - \psi_0) + \cos^2(i) \cos^2(\psi - \psi_0)] + R_c^2 \cos^2(i)}}, \quad (1)$$

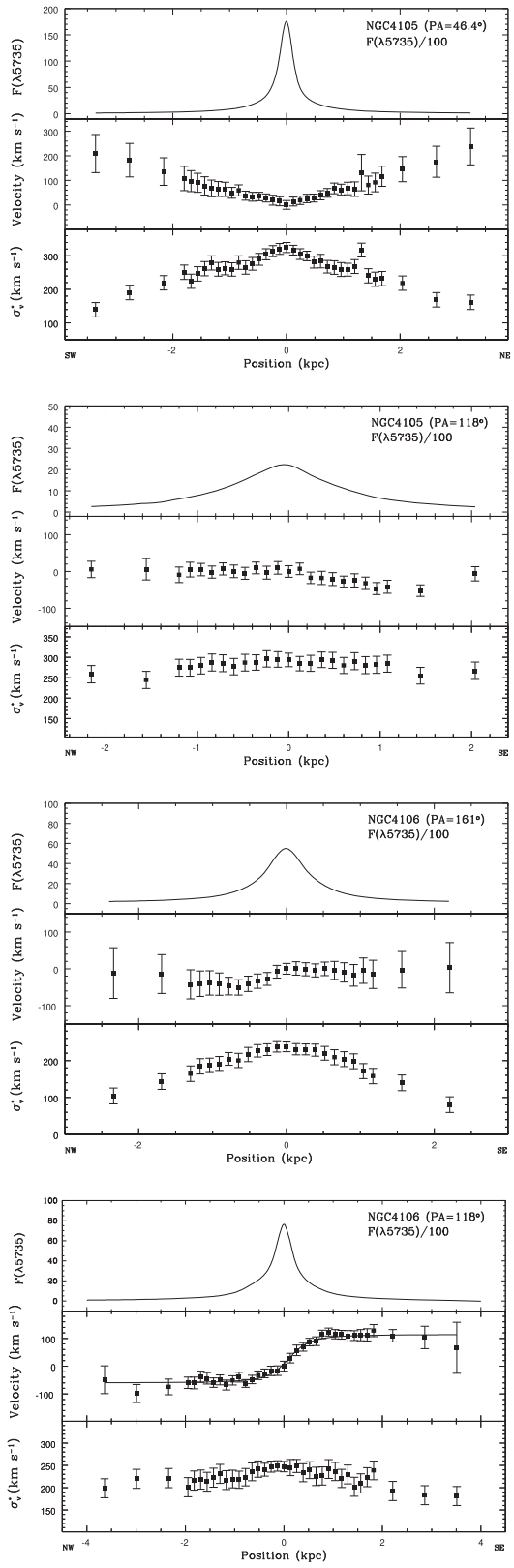

Figure 2. Spatial profiles of observed λ 5735 flux, in units of 10^{-17} erg cm^{-2} s^{-1} (top), radial velocities after subtraction of systemic velocities (middle), and velocity dispersion (bottom) for NGC 4105 and NGC 4106 along the different position angles, as indicated. The velocity scale was not corrected by the disc inclination.

where R is the radius in the plane of the galaxy, V_s is the systemic velocity, and V_0 and R_c are defined as amplitude parameters and the shape of the curve.

The inclination of NGC 4106 with respect to the plane of the sky, estimated as $i \sim 50°$, was determined using the observed axial ratio taken from Herrera-Endoqui et al. (2015). The position angle of the line of nodes, $\psi_0 = 91°$, was also taken from the same reference. From the fitting of the radial velocity observed for NGC 4106 (PA=118°), shown in the bottom panel of Fig. 2, we obtain a deprojected velocity amplitude of $V_0 = 138 \pm 6$ km s^{-1}. Supposing that the mass within a certain radius is given by $M(R) = RV_0^2/G$, using the amplitude of this fit, the dynamical mass of the S0 galaxy is about 1.6×10^{10} M$_\odot$ up to a radius of 3.64 kpc.

3.2 Gaseous kinematics

The gaseous radial velocity in NGC 4105 and NGC 4106 was determined using the task *emsao* (Mink & Wyatt 1995) implemented in the RVSAO package (Kurtz & Mink 1998). This program finds emission lines in a spectrum and computes the observed centre, yielding individual radial velocities and errors for each line and combining them into a single radial velocity. The program was successful at finding the emission lines [O II] 3727 Å and [N II] 6584 Å. The errors are estimated from the uncertainty in the dispersion function in Å and in the fit to the centre of the Gaussian. The velocity dispersion σ_v^{gas} and its error were calculated as a function of FWHM, measured using the splot task from IRAF. The FHWM uncertainty is estimated from the Poisson error. The velocity dispersion was corrected by the instrumental broadening $\sigma_{v,\,inst}$ (132 ± 5 km s^{-1}), where $\sigma_{line} \sim (c/2.352) \times \mathrm{FWHM_{line}}/\lambda_{central}$ and $\sigma^2_{line} = \sigma^2_v + \sigma^2_{v,inst}$. We assumed the radial velocity of the central aperture of each galaxy as the heliocentric velocity.

The radial velocity and velocity dispersion profiles of each observed slit position are shown in Fig. 3. The number of kinematic measurements of the gaseous component is smaller than the stellar component, reaching only the central kpc of galaxies.

As can be seen in the top panel of Fig. 3, NGC 4105 does not show a U-shaped radial velocity profile along PA = 46.4°, like that observed for the stellar kinematics. Gas velocity dispersions for this slit are lower than those of the stars, but the profile is similar, with a peak in the nuclear region and descending wings for both sides. The radial velocity profile across PA = 118° shows a clear rotational pattern, very different from the almost flat profile of the stellar component, considering our error bars (see Fig. 2). It should be noted that the slit did not cross the centre of the galaxy. The behaviour of ionized gas velocity profiles in both directions is very different from that of the stellar profiles, i.e. ionized gas and stars do not share the same dynamics.

The gaseous and stellar kinematics in NGC 4105 were previously studied by Caon et al. (2000), using long-slit spectroscopy and a similar methodology to ours. They observed with the slit positioned at PA = 156°, different from our slit position and also not coincident with the photometric major axis position angle (see Table 1, PA = 136.4°). Caon et al. (2000) also verified that the gas velocity curve shows a strong rotation pattern with peak velocities above 200 km s^{-1}. Their stellar velocities show a quite symmetric profile with positive velocities towards the NW direction and negative to the SE ($\lesssim$40 km s^{-1} for both sides), which they interpret as rotation. Based on it, they argue that the ionized gas in NGC 4105 is counter-rotating with respect to the stars, is of external origin, is not in equilibrium, and was acquired recently, also affecting the stellar kinematics. In the stellar velocity profile of our PA=118° slit

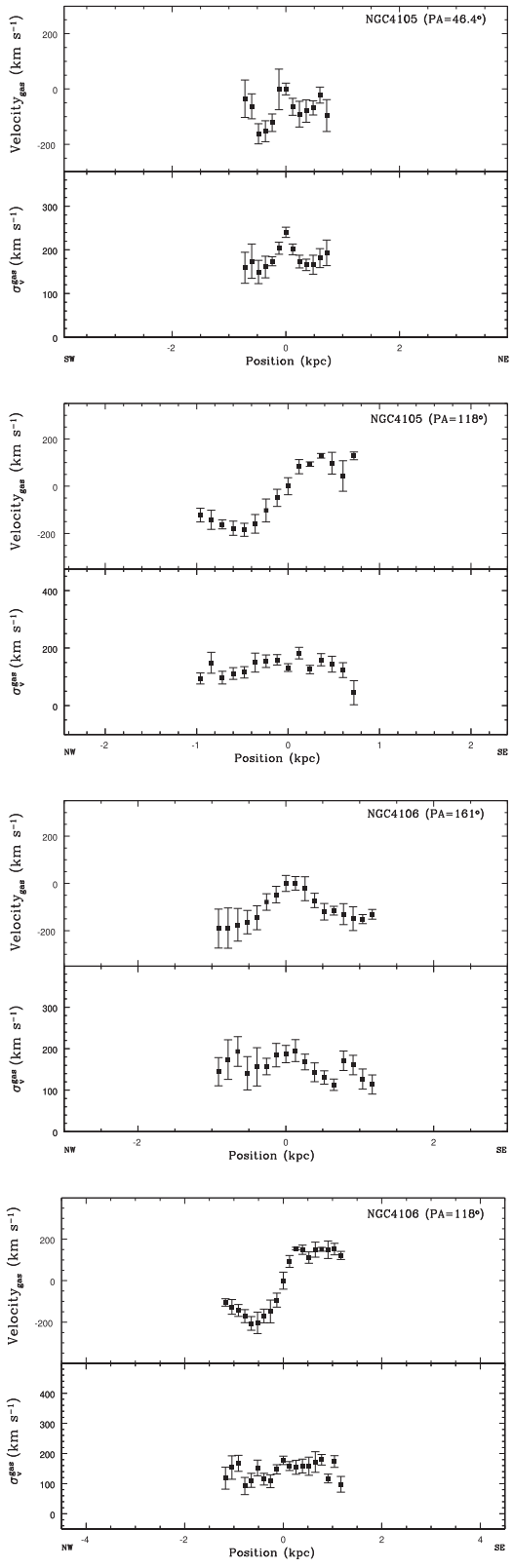

Figure 3. Radial velocity and velocity dispersion profiles for the ionized gas in NGC 4105 and NGC 4106 derived from [O II]3 727Å and [N II] 6584Å. Radial velocities were obtained after subtraction of the velocity in the central aperture, defined by the position of the flux peak in the spatial profile. As in Fig. 2, the velocity scale was not corrected for galaxy inclination.

position, we also observed counter-rotation (with a slightly lower velocity range), but our simulation fails to reproduce that. We show in Section 4 that the origin of this gas is not the current companion galaxy, as can be inferred from our simulation, in which no gas is transferred from NGC 4106 to NGC 4105.

We argue that the stellar velocity profile obtained by Caon et al. (2000) may reflect the transfer of orbital angular momentum to the outermost stars of NGC 4105 during the close encounter, in contrast to pre-existing rotation.

In NGC 4106, the radially symmetric velocity profile across the slits reaches a maximum velocity of 206 ± 33 km s^{-1} at ~ 0.65 kpc over PA=118°. The velocity dispersion profiles at both slits are very much steeper than the stellar profiles and nearly symmetrical up to $\sim$1.2 kpc, with a central value of 187 ± 21 km s^{-1} for PA=161° and 178 ± 14 km s^{-1} in the central aperture of PA=118°.

The H I gas masses for the galaxies were measured by Bottinelli & Gouguenheim (1979), who found $M_{\rm H\,I} = 5.2 \times 10^8$ M$_\odot$ for NGC 4105 and $M_{\rm H\,I} = 3.4 \times 10^8$ M$_\odot$ for NGC 4106.

4 *N*-BODY + SPH SIMULATIONS

Numerical simulations were carried out in order to reconstruct the interaction history between the galaxies NGC 4105 and NGC 4106. The simulations were performed using the TREEPM/SPH code P-GADGET3, an updated and significantly extended version of GADGET-2 (Springel 2005), where the dark matter and stars are followed by collisionless particles and gravity is calculated in a tree code. The gas is treated through Smoothed Particle Hydrodynamics (SPH: Springel & Hernquist 2002), with the star formation process, radiative cooling and feedback, and subgrid star formation model as defined in Springel & Hernquist (2003), from which we used the same parameters.

4.1 Initial conditions for the simulation

Based on the observational data presented here and elsewhere, we began to construct the initial conditions for our simulations. In the case of AM 1204−292, the collision is between an elliptical galaxy (NGC 4105) and an S0 galaxy (NGC 4106).

The total stellar masses of both galaxies were derived through the mass-to-light ratios resulting from stellar population synthesis (see Section 5). We correct the slit stellar mass obtained from STARLIGHT to the total stellar mass by scaling the total and slit luminosity in the B band. The total B-band luminosities were taken from the ESO-LV catalogue and are $L_B \sim 7.24 \times 10^{10}$ L$_\odot$ and $L_B \sim 5.62 \times 10^{10}$ L$_\odot$ for NGC 4105 and NGC 4106, respectively. Then the stellar masses are 1.81×10^{11} M$_\odot$ and 8.30×10^{10} M$_\odot$, for NGC 4105 and NGC 4106 respectively.

4.2 NGC 4105 model

The elliptical galaxy was modelled by two spheroidal Hernquist (1990) components, one for the stars, the other for the dark matter halo:

$$\rho(r) = \frac{M}{2\pi}\frac{r_{\rm h}}{r(r+r_{\rm h})^3}, \qquad (2)$$

where M is the total mass and a is the radial scalelength of each component. Two models were constructed: (i) the first one has a spherical stellar component within a concentric spherical dark matter halo to test the hypothesis that the gas present in this galaxy was stolen from NGC 4106 during collision, as will be discussed in Section 4.4;

Table 3. NGC 4105 (E with gas) model parameters.

	Phys. units*
NGC 4105 model (elliptical)	
Number of particles in halo	700 000
R_{200}	155 kpc
M_{200}	86.59×10^{10} M$_\odot$
V_{200}	155 km s^{-1}
r_h	23.4 kpc
Halo mass (M_{dm})	71.69×10^{10} M$_\odot$
Number of particles in stellar disc	200 000
Disc mass ($M_{d,s}$)	0.086×10^{10} M$_\odot$
Disc radial scalelength ($R_{d,s}$)	3.2 kpc
Disc vertical scale thickness ($z_{0,s}$)	0.63 kpc
Number of particles in gas disc	200 000
Gas disc mass ($M_{d,g}$)	0.064×10^{10} M$_\odot$
Gas disc radial scalelength ($R_{d,g}$)	3.2 kpc
Gas disc vertical scale thickness ($z_{0,g}$)	0.035 kpc
Number of particles in spherical stellar component	300 000
Spherical component mass (M)	14.72×10^{10} M$_\odot$
Spherical component radial scalelength (r_h)	4.77 kpc
Total mass of the model	86.59×10^{10} M$_\odot$
Total baryonic mass of the model	15.70×10^{10} M$_\odot$

Table 4. NGC 4106 (S0) model parameters.

	Phys. units*
NGC 4106 model (S0)	
Number of particles in halo	500 000
R_{200}	160 kpc
M_{200}	95.24×10^{10} M$_\odot$
V_{200}	160 km s^{-1}
r_h	32.35 kpc
Halo mass (M_{dm})	90.94×10^{10} M$_\odot$
Number of particles in stellar disc	450 000
Disc mass ($M_{d,s}$)	3.8×10^{10} M$_\odot$
Disc radial scalelength ($R_{d,s}$)	2.8 kpc
Disc vertical scale thickness ($z_{0,s}$)	0.56 kpc
Number of particles in gas disc	200 000
Gas disc mass ($M_{d,g}$)	0.064×10^{10} M$_\odot$
Gas disc radial scalelength ($R_{d,g}$)	2.8 kpc
Gas disc vertical scale thickness ($z_{0,g}$)	0.56 kpc
Number of particles in bulge	50 000
Bulge mass (M)	0.48×10^{10} M$_\odot$
Bulge radial scalelength (r_h)	0.56 kpc
Total mass of the model	95.52×10^{10} M$_\odot$
Total baryonic mass of the model	4.35×10^{10} M$_\odot$

(ii) stellar and gaseous discs were added to the second model, with exponential density profiles:

$$\rho(d) = \frac{M_d}{4\pi R_d^2 z_0} \exp\left(-\frac{R}{R_d}\right) \mathrm{sech}^2\left(\frac{z}{z_0}\right), \quad (3)$$

where M_d, R_d, and z_0 are the stellar or gaseous disc mass, radial scalelength, and vertical scalelength, respectively.

We start setting up our galaxy model using the values of mass. The stellar mass is presented in the previous section. For the halo model, we took typical parameters for elliptical galaxies. The first guess for the total mass (dark plus baryonic) was obtained using equation 4.249b from Binney & Tremaine (2008), based on the scalar virial theorem. The velocity dispersion is presented in Section 3.1 (Fig. 2), from PA =46.4°, which gave us a mass of $M \sim 5 \times 10^{11}$ M$_\odot$. The radial velocity curves are also used as observational beacons. During construction of the model galaxy, we should find a good set of parameters that are committed to observational data and still produce a dynamically stable model. The final value of the total mass is a little higher: $M_{200} \sim 8.7 \times 10^{11}$ M$_\odot$, as the stellar mass.

All galaxy models in the present article were set following the prescription given by Springel (2005). The spheroidal halo and bulge follow the Hernquist (1990) profile (equation 2), while the gas and stellar discs have an exponential density profile (equation 3). The parameters of the final model are given in Table 3.

4.3 NGC 4106 model

For NGC 4106, the S0-type galaxy, we started with the stellar mass derived from the *M*/*L* ratio obtained from stellar population synthesis (see Sections 4.1 and 5). For each model generated, we compared the rotation curve with the stellar radial velocity curves obtained from long-slit spectroscopy (Fig. 2). The slit position PA =161° crosses the galaxy through its nucleus, in a direction close to the galaxy minor axis (at PA =181°), so that no rotation is detected. The other one, at PA =118°, is close to the major axis direction (at PA =91°), but does not cross the galactic centre. Both radial velocity curves were corrected to estimate the rotation curve of the galaxy, as explained in Section 3.1. Then we generated a set of S0-like galaxy models, constructed with a bulge and a halo given by Hernquist (1990) spheroids (equation 2) and an exponential disc (equation 3). We plotted the corresponding rotation curve over the observed one and chose the one that best reproduced the mean observed rotation curve and is dynamically stable (i.e. it survives with its mass distribution nearly unaltered in a 1-Gyr run). It was not a fitting procedure. The parameters of the final NGC 4106 model are also given in Table 4.

Each galaxy model was evolved in isolation for 3 Gyr to test its stability and to allow numerical relaxation.

4.4 The orbit

In order to find the orbit followed by both galaxies, we wrote a code that takes as input parameters the distance to the galaxy pair, the positions of the galaxies projected in the sky plane, and the radial velocities of their mass centres. Then the algorithm calculates orbits that may lead to the present state of the system. Many thousands of orbits are presented. We then identify families of orbits and select those that, by morphological and kinematic constraints, are suitable to take the system to its present state. Then, a large series of low-resolution test simulations was run, out of which six best cases were chosen and run in higher resolution. Orbital parameters are presented in Table 5.

The simulation starts 1 Gyr before perigalacticum, with the galaxies at an initial distance of 1 Mpc. In this initial configuration, dark matter haloes are far enough from each other that the dynamical damage caused by the sudden presence of the other galaxy model is negligible. Galaxy models were evolved in isolation for 1 Gyr, before being stacked together for the collision run.

A whole set of simulations was performed using a simple elliptical galaxy model for NGC 4105 (spherical model with dark matter and stars), with the gaseous content of the pair placed entirely in the NGC 4106 model. Remember that both galaxies have a similar amount of H I gas, as stated at the end of Section 3.2. Despite being very successful in several aspects (reproduction of morphology, kinematics, consistent evolution of the star formation rate, etc.), the model failed in one respect: there was no gas transfer from NGC 4106 to NGC 4105. From this result, we can be sure that, as already suggested by Caon et al. (2000), the gas present in NGC 4105 is pre-existing and must have been captured in a previous event.

Table 5. Orbital parameters from the best model.

	Phys. units*
NGC 4106 model (S0)	
Eccentricity	0.9
Pericentre distance	5.7 kpc
Present distance	17.7 kpc
V_{sys}	$-329\,km\,s^{-1}$
Pericentre vector direction*	(0.004, 0.961, −0.275)
Orbital plane normal vector direction**	(0.356, −0.871, −0.338)
Present-day position vector*	(−8.8, −4.2, −14.8) kpc
Present-day velocity vector*	$(-792, -91, -329)\,km\,s^{-1}$
Initial galaxy separation	1.0 Mpc

Notes. *Vector components defined in a Cartesian reference frame (*X*, *Y*, *Z*) centred on NGC 4105, with *X* to the north, *Y* to the west, and *Z* in the line-of-sight direction, with positive values towards the observer.
**The orbital plane normal vector is the direction of the orbital angular momentum (reference frame defined as in *).

Then, the second set of simulations was run with stellar and gaseous discs added to the NGC 4105 model. It makes sense in view of the results by Grützbauch et al. (2009), who found dusty features in the central region and modelled the brightness distribution, concluding that it presents a discy outer structure. The subtraction of their model showed a central bar-like structure. From the best-fitting simulation out of this set, we present in Fig. 4 different renderings of the snapshots that reproduce the current situation of the system, 14.2 Myr after perigalacticum. The main morphological features, such as the general shape and the tidal arms, are well reproduced by the simulation. In the last panel of Fig. 4 we show the gas discs from a viewpoint different from our line of sight. The discs are completely disconnected, with no bridges, connecting tails, or stream between them, showing that no gas is transferred from one galaxy to the other.

The velocity distribution, measured by long-slit spectroscopy, can also be compared directly with the velocity map extracted from the simulation at the current system state. It is presented in Fig. 5, where only the stellar discs are shown.

Fig. 6 shows the time evolution around perigalacticum (at 1.311 Gyr after the beginning of the simulation) of the star formation rate (SFR) during the simulation. Note that just after perigalacticum a sudden peak in SFR occurs, as expected. We plotted the SFR evolution of the isolated models in orange to show that the peak is due to collision. At the moment, the system is undergoing an outbreak of star formation. In Section 5 we present the stellar population synthesis, from which we detect, in some apertures and for both galaxies, the presence of a few per cent of the young stellar population. The star formation rate peaks near 60 Myr after perigalacticum, with an SFR of $0.12\,M_{\odot}\,Myr^{-1}$.

Regarding the radial velocity distribution (Fig. 5), it also corresponds nicely with the observed velocities over the slit positions. If we take the velocity profile along PA=46.4° from the velocity map, we will have a beautiful U-shaped profile, unlike what happens along the line that connects the nuclei of the galaxies.

The velocity profile along PA = 118° is presented in Fig. 7. The overall shape of the velocity profile taken from the simulation is in good agreement with the observed one. At the left end of the graph, which corresponds to the SE side of the slit, the velocity in the simulation keeps rising to values above $300\,km\,s^{-1}$, while the observed profile becomes flat at $\sim 250\,km\,s^{-1}$. This is due to the details in that part of the simulated galaxy, which develops a prominent bar, stronger than that in NGC 4106. On the other side, the velocity profile in the NGC 4105 section is quite strange, with a low-velocity tail in the direction of its companion galaxy. It is clear that a simulation can hardly reproduce the observations with a very high degree of detail. Both simulations and observations have limiting factors that affect the data. The objective here is to study the dynamics along general lines.

5 STELLAR POPULATIONS SYNTHESIS

To compute the stellar population contribution to the galaxy pair, we utilized the STARLIGHT stellar population synthesis code (Cid Fernandes et al. 2005). Full details of the code and methodology are discussed in Cid Fernandes et al. (2004, 2005, 2007), Mateus et al. (2006), and Asari et al. (2007). Briefly, the code fits the observed spectrum (O_λ) in terms of the overlap of simple stellar population synthesis models (SSPs) with a wide range of ages and metallicities. In this code, we adopt the empirical stellar spectral library by Bruzual & Charlot (2003). The library includes spectra with a spectral resolution of 3 Å (FWHM) over a wavelength range λλ3200–9500 Å under a sampling of 1 Å. We also adopted the Padova 1994 tracks and an initial mass function (IMF) by Chabrier (2003) for stars with masses between 0.1 and 100 $M_{\odot}$.

The basic equation of the synthetic spectrum solved by STARLIGHT is given by

$$M_\lambda / M_{\lambda_0} = \left[\sum_{j=1}^{N_\star} \boldsymbol{x}_j b_{j,\lambda} r_\lambda \right] \otimes G(v_\star, \sigma_\star), \quad (4)$$

where M_{λ_0} is the synthetic flux at that rest-frame wavelength; $\boldsymbol{x}_j$ is the population vector; $b_{j,\lambda}$ is the reddened spectrum of the *j*th SSP model that is flux-normalized at $\lambda_0 = 5750$ Å; $r_\lambda \equiv 10^{-0.4(A_\lambda - A_{\lambda_0})}$ is the extinction term; ⊗ represents the convolution operator; $G(v_\star, \sigma_\star)$ denotes a Gaussian distribution along the line of sight centred at velocity $v_\star$ and with a star velocity dispersion $\sigma_\star$. The population vector $\boldsymbol{x}$ denotes the percentage contribution of the SSPs at λ_0 weighted by flux, expressed in terms of age and metallicity (t_j, Z_j). The population vector can also be expressed as a function of the SSP mass fractional contribution and is denoted by the vector $\boldsymbol{m}$.

The goodness of fit between the observed and synthetic spectra is derived from an algorithm that finds the results for the minimum value of (χ^2). The intrinsic reddening is modelled by the code as due to light scattering by dust, adopting the extinction law of Cardelli, Clayton & Mathis (1989). The SSPs considered in this work take into account 15 ages ($t = 0.001$, 0.003, 0.005, 0.01, 0.025, 0.04, 0.1, 0.3, 0.6, 0.9, 1.4, 2.5, 5, 11, and 13 Gyr) and three metallicities ($Z = 0.2$, 1, and $2.5\,Z_{\odot}$), summing up $N_\star = 45$ SSP components.

We combined the individual components in age bins following the prescription of Cid Fernandes et al. (2005) as a young stellar population, x_y or m_y ($t < 1 \times 10^8$ yr), intermediate stellar population, x_i or m_i ($1 \times 10^8 \leq t \leq 1 \times 10^9$ yr), and old stellar population, x_o or m_o ($t > 1 \times 10^9$ yr). These components are employed to construct the SSPs with their flux ($\boldsymbol{x}$) and mass ($\boldsymbol{m}$) fractional contributions.

Another important point is that the STARLIGHT code usually does not provide the uncertainties of the resulting parameters. However, we estimated the uncertainties of the average parameters as a function of the spectrum quality indicated by signal-to-noise ratio (SNR) variations. For this, we applied 20 levels of random flux perturbations over the central spectrum of each slit position observed and calculated the percentage differences between the new estimates and standard ones. These percentage differences were scaled to the other apertures of the slit according to the SNR of the spectrum considered. We considered only spectra with a good quality SNR of the continuum (at least 10).

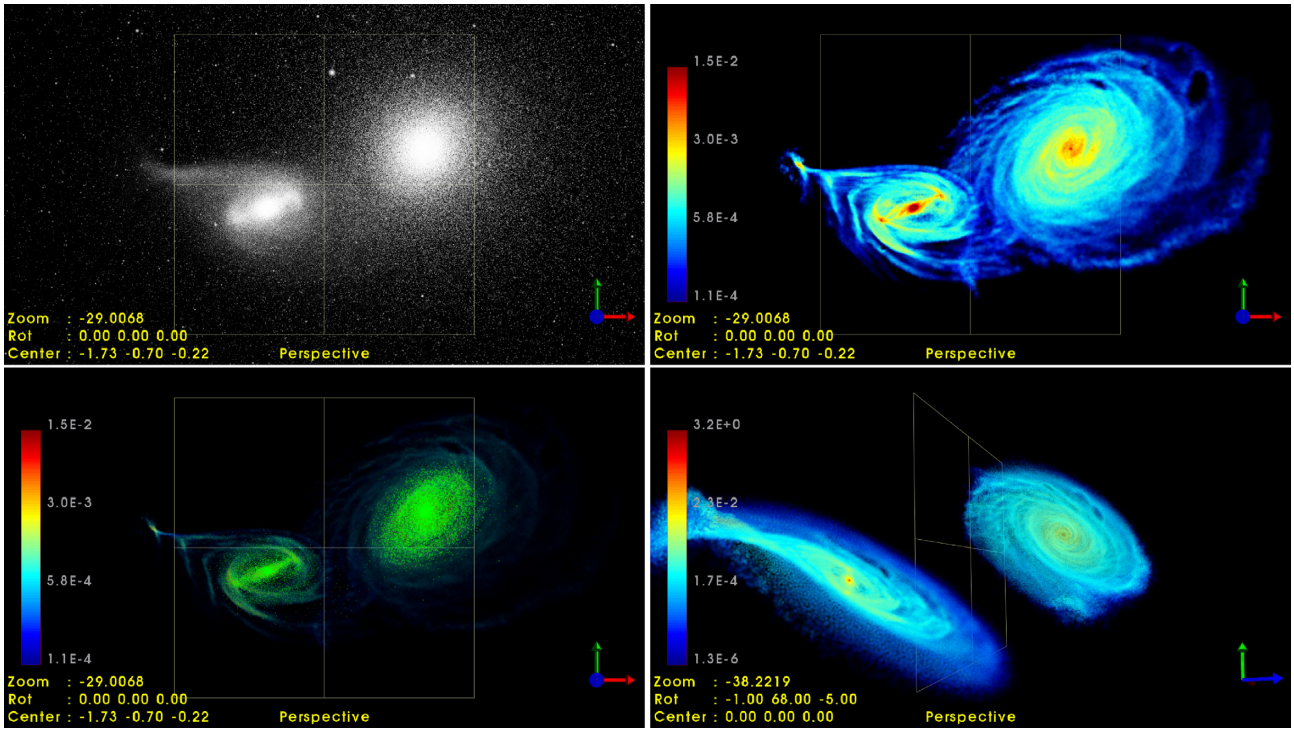

Figure 4. Selected views of the snapshot that best reproduces the observed kinematics and morphology of AM 1204−292, 14.2 Myr after perigalacticum. Top left panel: only stellar particles are shown. Top right: gas density distribution. Bottom left panel: stars formed during the simulation are drawn in green over the gas distribution. Bottom right panel: the gas distribution viewed from a different view point to show that the galaxies are completely detached from each other, with no connecting bridges. No gas is transferred between galaxies. The square grid at the centre of each panel is 20 kpc wide.

In Fig. 8 we present some examples of the results of the spectral synthesis fitting for the central and outskirt regions of NGC 4105 and NGC 4106. The results of stellar population synthesis for the individual spatial bins across the slit positions are shown in Fig. 9, stated as the fractional contribution of each base element weighted by flux and mass. It can be noted that the spatial distributions of stellar populations are homogeneous across all slit positions. NGC 4106 is a kind of lenticular galaxy, so we would expect to find a light-weighted stellar age a few billion years lower than in the elliptical galaxy NGC 4105. From the simulation, the maximum fraction of young stellar population ($\leq$30 Myr) in NGC 4105 would be 3.8 per cent. What we actually found for both galaxies was that the stellar population in both galaxies is composed predominantly of the old component in light, as well as in mass, with a very small fraction (up to 5 per cent) of young and intermediate populations, very close to the detection threshold of the stellar population synthesis method.

We show in Fig. 10 the light-weighted means of stellar age and metallicity as a function of the linear distance towards the nucleus in each observed galaxy (expressed in kpc). The age (in Gyr) is presented on a logarithmic scale and the metallicity Z on a logarithmic scale normalized to the solar value, i.e. $\log(Z/Z_{\odot}) = [Z]$, for which $Z_{\odot} = 0.02$ to be consistent with the adopted SSP grid. The stellar population synthesis has extracted light-weighted stellar age and metallicity in two distinct projected directions for each galaxy, across which we have also measured the stellar kinematics (see Section 3.1). The stellar population properties have been derived from a set of aperture spectra along radial distances up to almost $0.5R_{\rm e}$ in the case of NGC 4105 and up to around $1R_{\rm e}$ for NGC 4106. NGC 4105 is morphologically classified as an E3 galaxy and NGC 4106 as an SB(s)0 + galaxy, i.e. a lenticular barred galaxy. Specifically, for NGC 4106, our kinematics observations have shown that the slit direction at PA = 118° is more aligned to a stellar rotating disc than that at PA = 161°, at which the maximum line-of-sight rotational velocities are $128 \pm 22\,{\rm km\,s^{-1}}$ and $50 \pm 21\,{\rm km\,s^{-1}}$ respectively (see Fig. 2). The other galaxy, the elliptical NGC 4105, does not exhibit any stellar rotating disc. Since the radial variations of both stellar properties are indistinguishable across both directions in each observed galaxy, we have aggregated them all for each object into a single dataset in order to estimate representative radial gradients of light-weighted stellar age and metallicity. The stellar properties derived for different apertures on each side of the radial profile across two distinct projected directions were averaged in the case corresponding to the same nuclear distance within 1 arcsec; otherwise, the apertures are considered individually. The radial distances of all apertures towards the galaxy nucleus were corrected by the inclination angle of the reference plane of each corresponding galaxy.

In the case of NGC 4105 (a massive E3 galaxy), we have measured, up to a nuclear distance of about 4.6 kpc (i.e. up to around $0.45R_{\rm e}$), a slightly negative gradient in age ($\Delta\log(\text{age (Gyr)})/\Delta R(\text{kpc}) = -0.018 \pm 0.002\,\text{dex kpc}^{-1}$ and $\Delta\log(\text{age (Gyr)})/\Delta\log(R(\text{kpc})) = -0.051 \pm 0.012$) and a very sharp negative metallicity gradient ($\Delta\log(Z/Z_{\odot})/\Delta R(\text{kpc}) = -0.070 \pm 0.006\,\text{dex kpc}^{-1}$ and $\Delta\log(Z/Z_{\odot})/\Delta\log(R(\text{kpc})) = -0.210 \pm 0.023$). Whilst the variation in stellar age is very small (i.e. from nearly 13 Gyr in the nucleus down to around 11 Gyr at about $0.5R_{\rm e}$), the metallicity decreases strongly from about $[Z] = +0.1$ dex in the nucleus down to nearly $[Z] = -0.2$ dex at about $0.5R_{\rm e}$.

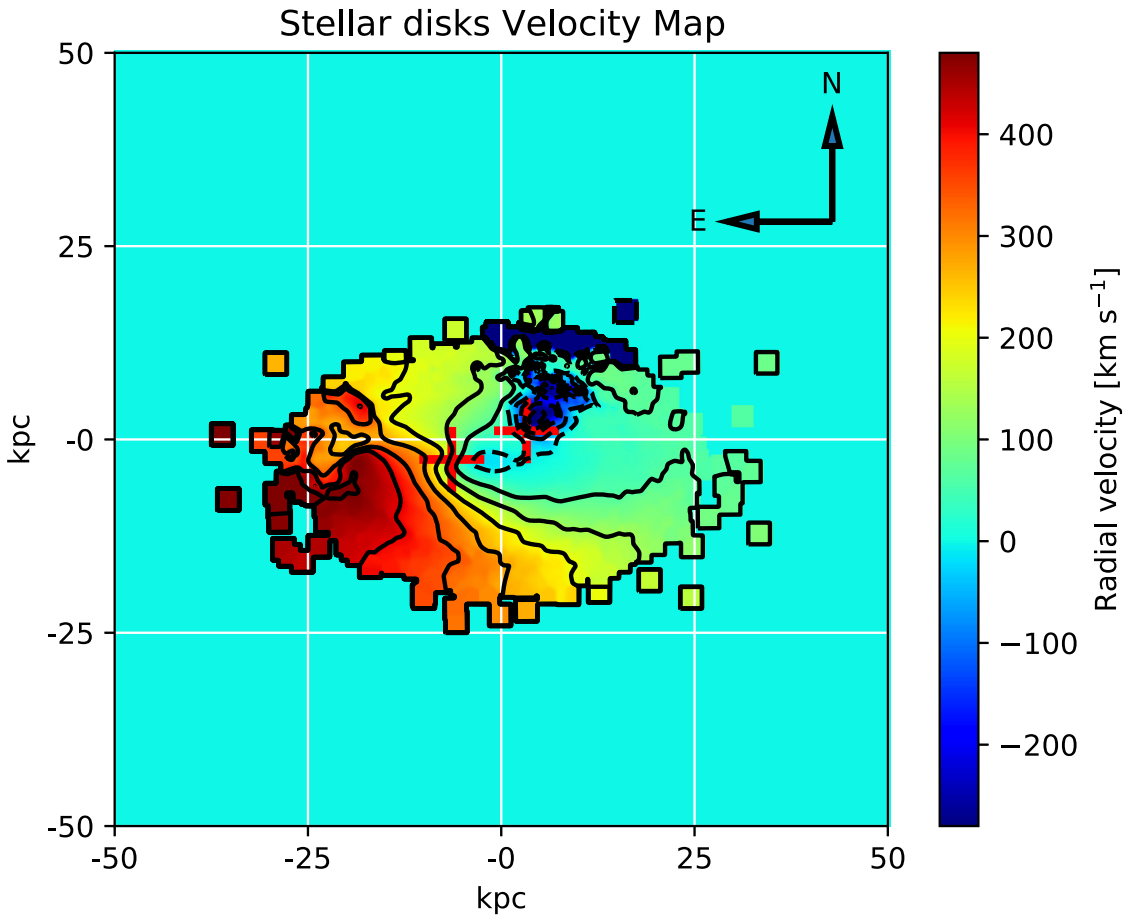

Figure 5. Stellar radial velocity map of the snapshot that best reproduces the observed kinematics and morphology of AM 1204−292, 14.2 Myr after perigalacticum. Only disc components of both galaxies are shown. Red crosses mark the centre of each model galaxy.

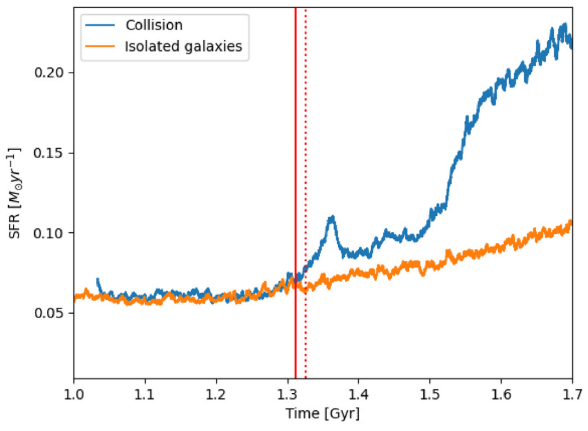

Figure 6. Star formation rate evolution. Time is given in Gyr from the beginning of the simulation. The blue line shows the SFR in the encounter simulation. In orange we plot the sum of the SFR of the S0 and E galaxies when evolved isolated. Perigalacticum is at 1.311 Gyr (vertical solid red line), where a sudden star formation episode begins. The dotted vertical line at 1.325 Gyr marks the present state of the system, indicating that the SFR is rising due to the collision and will peak about 60 Myr after perigalacticum.

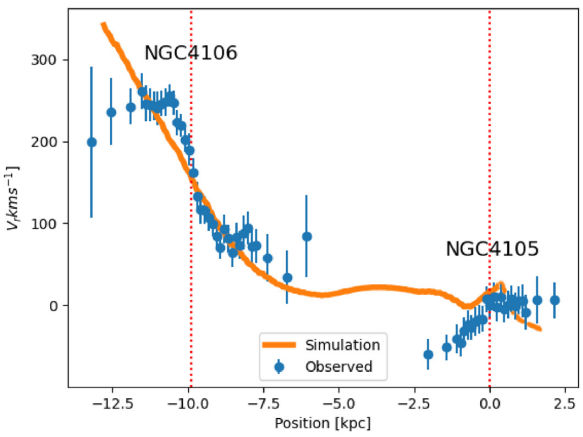

Figure 7. Velocity profile along PA = 118°. The observed data points are plotted in blue. In orange is a cut on the velocity map of the simulation (Fig. 5), over the same direction. The centre of each galaxy is indicated by the dotted vertical red lines.

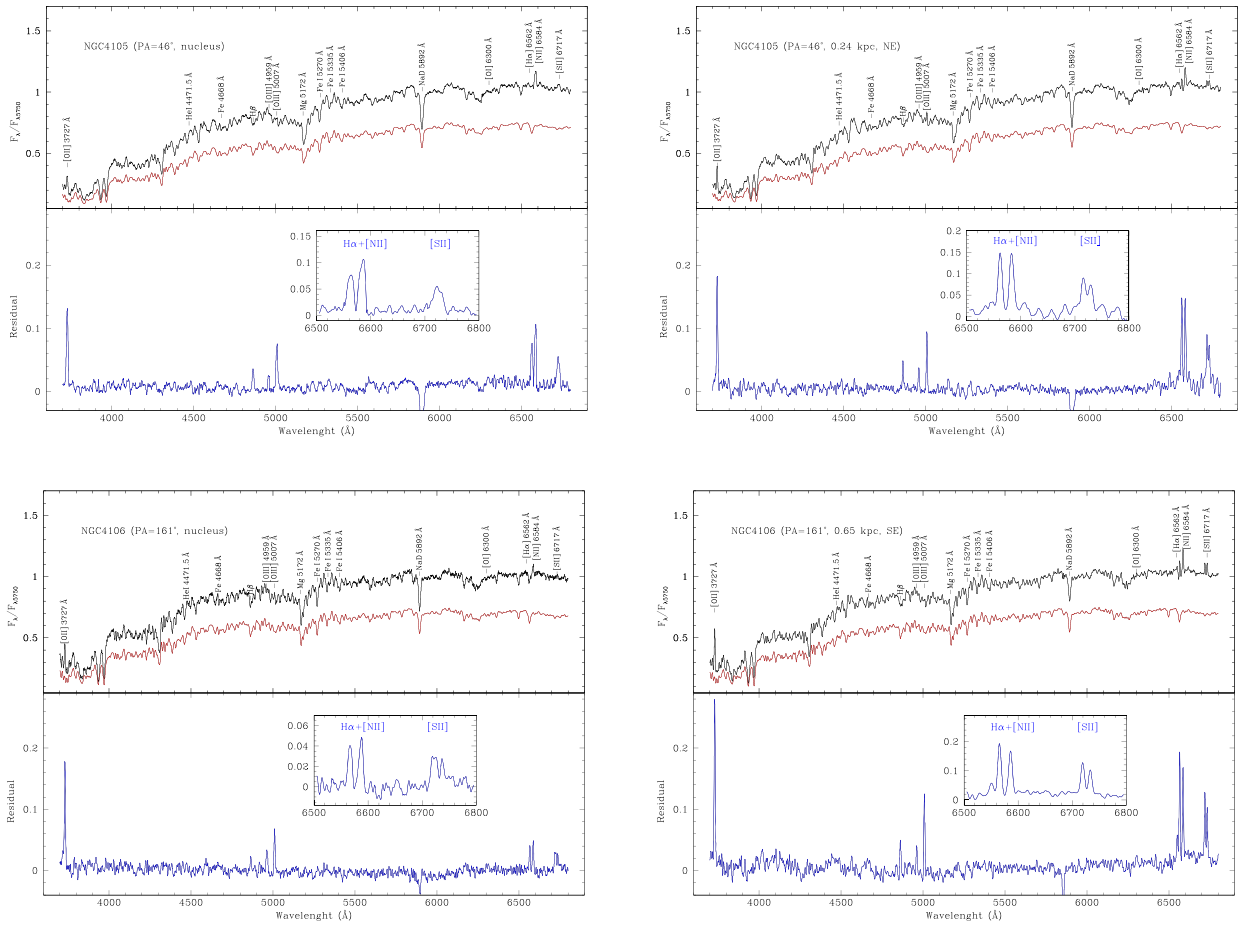

Figure 8. Stellar population synthesis for different regions of NGC 4105 (top) and NGC 4106 (bottom). The observed spectrum (black), the synthesized spectrum (red), and the residual spectrum, with its pure emission-line structure (blue), are shown. The main emission and absorption lines are identified, and an enlargement of the region between 6500 and 6800 Å is shown.

In the case of NGC 4106 (an intermediate-mass lenticular galaxy), we have measured nearly up to 3.4 kpc along the nuclear distance (i.e. up to about $1R_e$) a null gradient in age ($\Delta\log(\text{age (Gyr)})/\Delta R(\text{kpc}) = -0.010 \pm 0.005\,\text{dex kpc}^{-1}$, $\Delta\log(\text{age (Gyr)})/\Delta\log(R(\text{kpc})) = -0.028 \pm 0.015$) and a negative metallicity gradient ($\Delta\log(Z/Z_\odot)/\Delta R(\text{kpc}) = -0.045 \pm 0.008\,\text{dex kpc}^{-1}$ and $\Delta\log(Z/Z_\odot)/\Delta\log(R(\text{kpc})) = -0.114 \pm 0.027$). Whilst the stellar age is constant around 12.6 Gyr inside $1R_e$ ($\pm$0.6 Gyr), the metallicity decreases from around the solar value in the nucleus ($+$ 0.03 dex indeed) down to nearly $[Z] = -0.1$ dex at about $1R_e$ ($-$0.12 dex indeed), which corresponds closely to one third of the whole metallicity variation at a normalized radial distance two times greater in comparison with NGC 4105.

Negative gradients in stellar age and metallicity with different intensities are observed in massive early-type galaxies (especially ellipticals: Sánchez et al. 2012; González Delgado et al. 2015; Zibetti et al. 2020), such that older metal-richer stars are found within the innermost regions of the galaxy and relatively younger and metal-poorer stars in the outskirts, as a result of a long two-phase process (Oser et al. 2010). The initial phase occurs at high redshift and builds up the main body of the elliptical, with stellar populations evolving passively afterwards. In the second phase, lasting billions of years, minor/major dry mergers make the main body progressively bigger and redder. An extended relatively younger stellar envelope with relatively smaller metallicity than the nuclear region is also formed (Obreja et al. 2013; Huang et al. 2016). Very recently, Zibetti et al. (2020) investigated and compiled the spatial distribution of the light-weighted mean stellar age and metallicity inside extended galactic regions (i.e. up to $2R_e$) in a wide variety of nearby ETGs (48 E and 21 S0 extracted from the Calar Alto Legacy Integral Field Area Survey (CALIFA) integral field spectroscopic survey). They found that the age profiles typically follow a U-shaped variation in the plane log(age(Gyr))–R_e with a minimum around $0.4R_e$, increasing asymptotically outwards beyond $1.5R_e$ and increasing towards the nucleus. The greater the σ_v within $1R_e$ (σ_e), the smaller the depth of the minimum and the central increment, i.e. the flatter the age gradient. The metallicity gradients are found to be universally negative and strong, such that the metallicity flattens out moving towards larger radial distances (about -0.3 dex per $1R_e$ within $1R_e$). They analysed the metallicity profiles over the plane $\log(Z/Z_\odot)$–$\log(R_e)$. They state that a possible qualitative interpretation for their observations is a two-phase scenario for the formation of ETGs.

In comparison with the age and metallicity radial gradients investigated by Zibetti et al. (2020) in the most massive elliptical galaxies (i.e. $\sigma_e \geq 210\,\text{km s}^{-1}$), NGC 4105 exhibits, within the central region

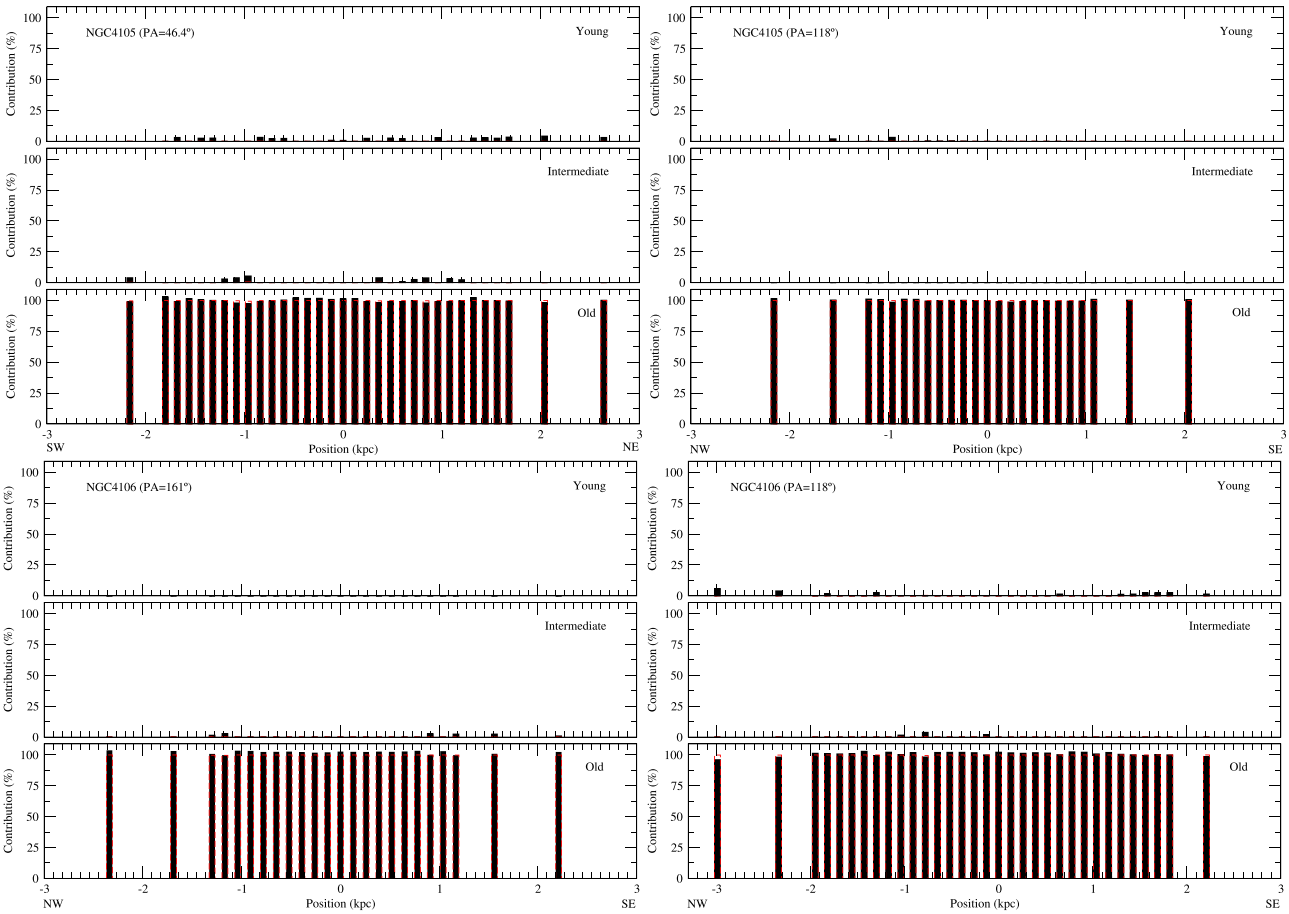

Figure 9. Flux and mass fractions (black and red bars, respectively) of SSP contributions from the best solution of STARLIGHT population synthesis.

up to $0.5R_e$, a comparable change in age and a greater variation in metallicity. In the case of NGC 4106, this SB0 galaxy presents, within the central region up to $1R_e$, smaller variations in both age and metallicity in comparison with ETGs with intermediate mass (i.e. $170 \leq \sigma_e < 210\,\mathrm{km\,s^{-1}}$).

Since the nearest approach between the galaxies seems to have happened only 30 Myr ago, we suppose the gradients of age and metallicity in both galaxies have not yet been substantially modified by the interaction in course. Both galaxies might have preserved their intrinsic stellar population spatial distributions according to their particular mass assembly histories. In fact, Kobayashi (2004) stated that the merging histories of elliptical galaxies could, in principle, be extracted from the observed metallicity gradients in local Universe galaxies. Kobayashi (2004) obtained that there is no correlation between the metallicity gradient and galaxy mass, based on a variety of chemodynamical simulations of elliptical galaxies (GRAPE-SPH code). An average gradient in metallicity that Kobayashi (2004) compiled was $\Delta\log(Z)/\Delta\log(R/R_e) = -0.3$ (± 0.2 as dispersion). Kobayashi (2004) also concluded that E galaxies that hypothetically were formed through a monolithic process would have steeper gradients, while E galaxies that undergo major mergers would have shallower gradients.

The stellar population synthesis has provided small flux contributions of young and intermediate-age populations (with age <100 Myr and 100 Myr $\leq$ age $\leq$1 Gyr respectively) in both galaxies, i.e. up to about 6 per cent, which is very close to the detection limit of stellar population synthesis applied through the STARLIGHT code. Therefore, these very small contributions did not represent any significant perturbation to the age and metallicity radial gradients. However, Grützbauch et al. (2007) argue that NGC 4106 shows a value for the H + K (Ca II) line-strength index larger than 1.3, i.e. larger than the maximum value attainable in post-starburst models (with both solar and supersolar metallicity), which suggests the presence of Hε in emission, considered a good indicator of recent star formation. The detection of [O II] λ3727, 3729 emission in the nucleus of NGC 4105 is also suggestive of a recent star formation episode.

On the one hand, in strongly interacting galaxies in which there was some reservoir of cold gas to form new stars during a long period of time, the metallicity gradient becomes significantly flatter than those observed in isolated galaxies, as shown for instance by Krabbe et al. (2008, 2011), Kewley et al. (2010), Bresolin et al. (2009), and Rosa et al. (2014). The shallow metallicity gradients found in strongly interacting galaxies could be explained as interaction-induced gas flows from the outer parts to the centre of each component (Toomre & Toomre 1972; Dalcanton 2007). On the other hand, the observed galaxy pair is under a strong interaction too, taking into account that the galaxies likely had a single encounter a few tens of millions of years ago and there was no great amount of cold gas available, so no significant star formation was actually induced inside both components by the mutual interaction.

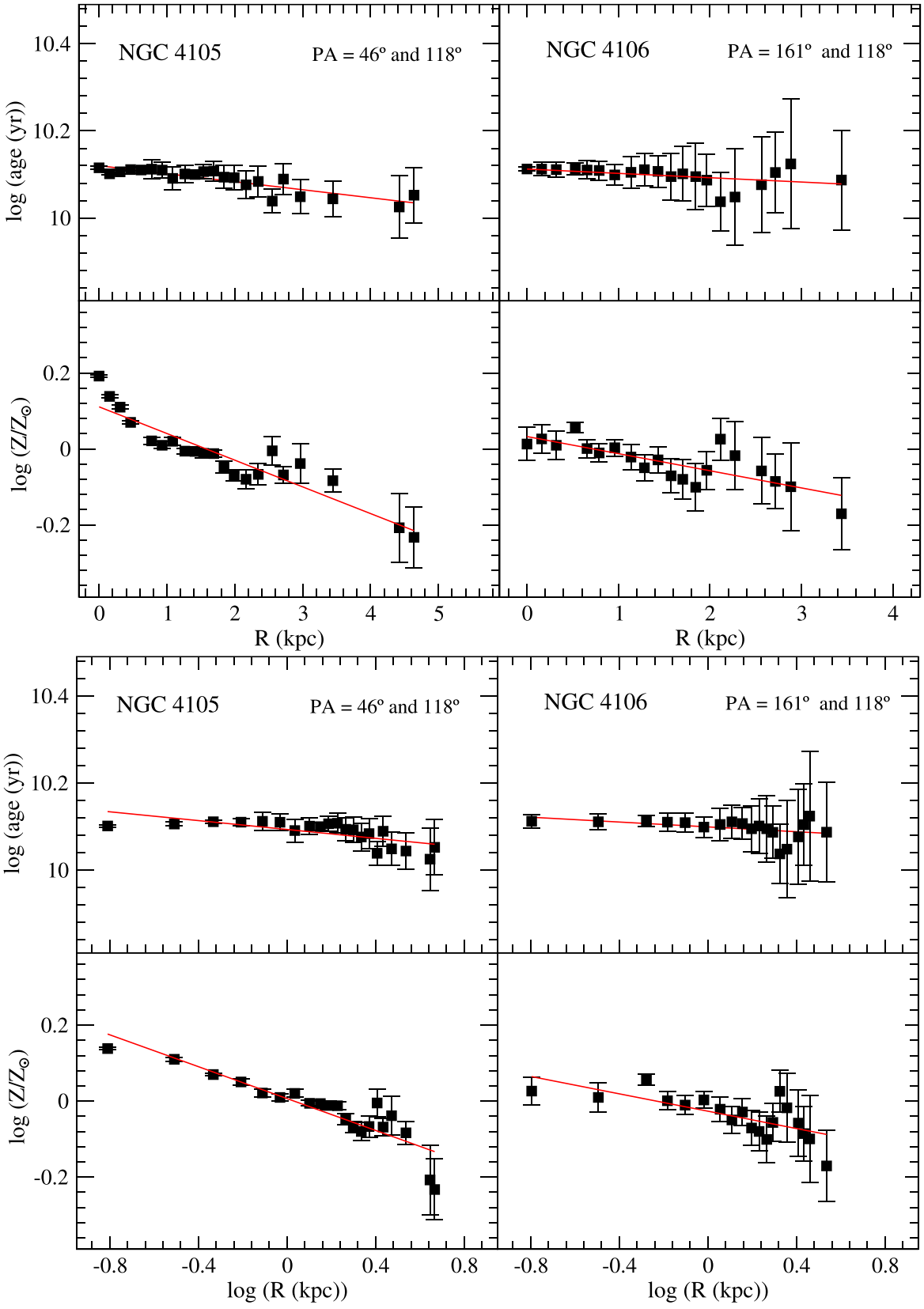

Figure 10. The mean stellar age and metallicity (both in logarithmic scales) as weighted by the flux contribution of SSP models addressed by stellar population synthesis as a function of the linear nuclear distance *R* (in kpc) and its logarithm, for NGC 4105 and NGC 4106.

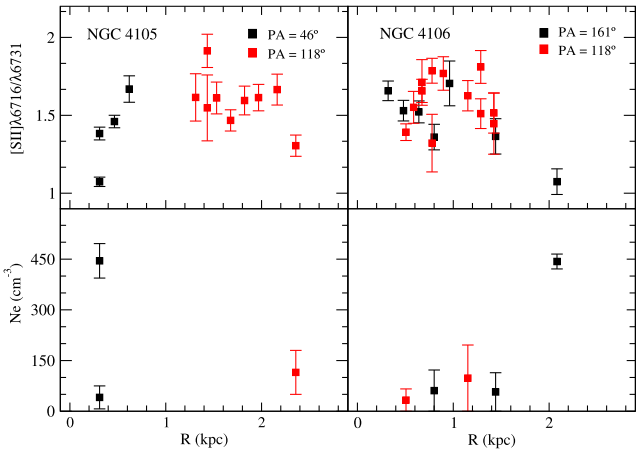

Figure 11. [S II] λλ6716/6731Å line ratio and electron density (N_e) as a function of linear radial distance in kpc.

6 IONIZED GAS PROPERTIES

The presence of emission lines is not unique to star-forming galaxies, but may also appear in early-type galaxies (e.g. Macchetto et al. 1996; Caon et al. 2000; Rosa et al. 2018; Diniz, Riffel & Dors 2018). Several studies have shown that line emission is prevalent in more than 50 per cent of passive red galaxies (Phillips et al. 1986; Goudfrooij et al. 1994; Yan et al. 2006; Capetti & Baldi 2011) and many early-type emission-line galaxies show the characteristic spectra of a LINER (Heckman 1980). As can be seen in Fig. 8, after the subtraction of the modelled stellar spectrum from the observed one, the pure nebular spectra in both galaxies present pronounced emission lines: [O II] λ3727, Hβ, [O II] λλ4959,5007, [N II] λλ6548,6584, Hα, and [S II] λλ6716,6731. In fact, previous studies have already detected some emission lines in the elliptical galaxy NGC 4105. For example, for NGC 4105, Longhetti et al. (1998) detected [O II] λ3727 and Caon et al. (2000) measured [N II] λ6584.

The line intensities were determined from fitting Gaussian profiles to the pure emission spectra, using the *splot* task in the noao.onedspec package of IRAF. The associated error for each line flux was given as $\sigma^2 = \sigma^2_{\rm cont} + \sigma^2_{\rm line}$, where $\sigma_{\rm cont}$ and $\sigma_{\rm line}$ are the continuum root-mean-square (rms) and Poisson error for the line flux, respectively. We corrected the observed line intensities for the effect of interstellar extinction. This was performed by comparing the observed Hα/Hβ ratio with the theoretical value of 2.86 from Pengelly (1964), for an electron temperature of 10 000 K. The starburst extinction law of Calzetti, Kinney & Storchi-Bergmann (1994) was adopted.

6.1 Electron density

We have determined the electron density (N_e) from the observed [S II] λ6716/λ6731Å ratio, using the *temden* routine of the NEBULAR package of STSDAS/IRAF, assuming an electron temperature of 10^4 K, since the lines sensitive to temperature were not observed in both galaxies. It is important to note that some regions in both galaxies present a [S II] ratio near the low-density limit, and therefore the electron densities for these areas cannot be estimated.

The radial profiles of the [S II] line ratio and N_e are plotted in Fig. 11 as a function of the linear radial distance for NGC 4105 and NGC 4106. The values of electron density obtained for both galaxies are in the range N_e = 33–445 cm^{-3} . These estimations are in agreement with those obtained by Krabbe et al. (2014) and Mora et al. (2019) for H II regions of interacting galaxies, which are systematically higher than those derived for isolated galaxies, N_e = 40–137 cm^{-3}, as previously estimated by Krabbe et al. (2014).

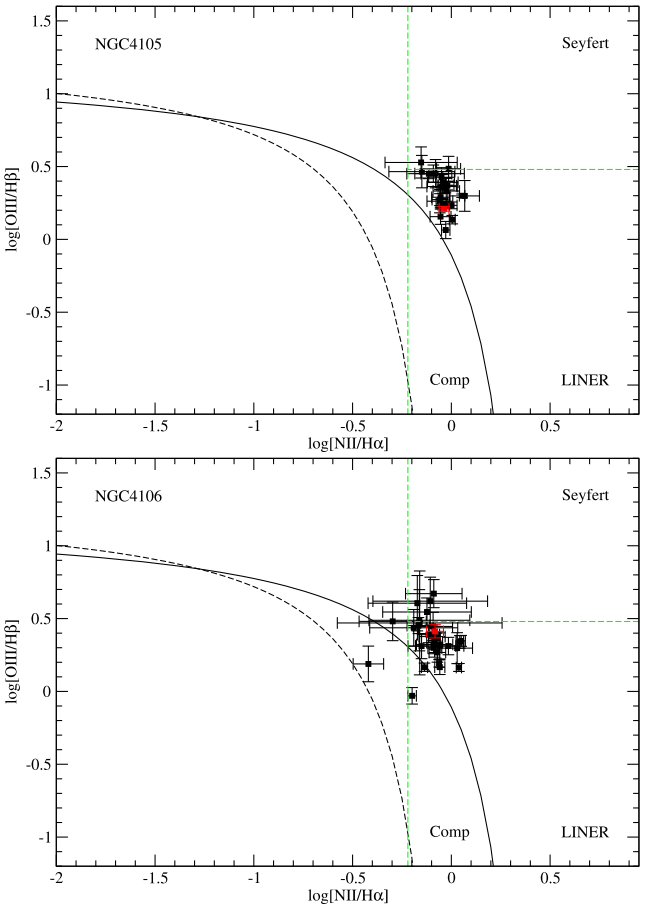

Figure 12. The [O III]/Hβ versus [N II]λ/Hα diagnostic diagram. The central region of each galaxy is marked by red symbols. The solid black line represents the theoretical upper limit for SF galaxies from Kewley et al. (2001) (Ke01), and the black dashed curve is the pure star-formation line from Kauffmann et al. (2003) (Ka03). The region between Ke01 and Ka03 is nominated as the composite region. The dividing line between Seyferts and LINERs (long-dashed, green) was set by Ho, Filippenko & Sargent (1997).

6.2 Oxygen abundance

The identification of the dominant ionization source for emitting gas across the galaxy is essential to determine the chemical abundance correctly. The elliptical galaxy, NGC 4105, is classified as a LINER galaxy by Mauch & Sadler (2007) and Véron-Cetty & Véron (2010) and NGC 4106 does not have a classification in the literature. Therefore, with the goal of confirming the ionization source of NGC 4105 and classifying NGC 4106, we used the [O III]/Hβ versus [N II]/Hα diagnostic diagram proposed by Baldwin, Phillips & Terlevich (1981), commonly known as the BPT diagram. This diagram is used to distinguish objects ionized by massive stars (SFs), AGNs, and LINERs. In our case, we cannot use [O III]/Hβ versus [S II]/Hα because the [S II] λλ6716,6731 emission lines presented a very low S/N in the central regions of the galaxies.

Fig. 12 presents the BPT diagram for regions measured along the different slit positions of AM 1204−292. We note that all

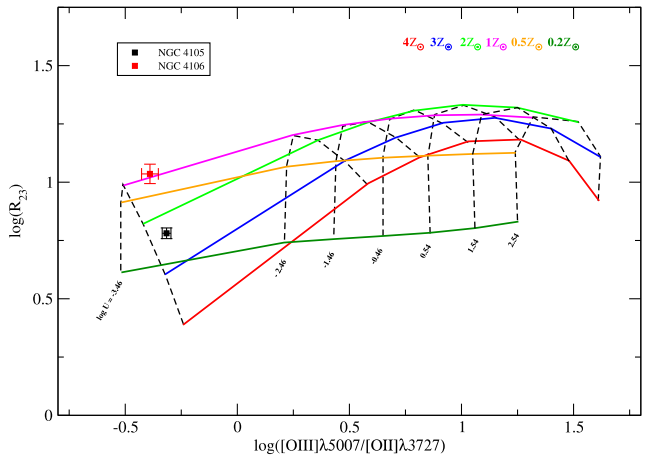

Figure 13. The $\log(R_{23})$ versus $\log([\mathrm{O\,III}]/[\mathrm{O\,II}])$ index. The dashed lines connect the photoionization model curves with different values of the logarithm ionization parameters, while the solid lines show different gas-phase metallicity. Black and red squares correspond to the nuclear regions in NGC 4105 and NGC 4106, respectively.

regions of NGC 4105 present LINER-like emission, in agreement with the findings of De Vaucouleurs et al. (1991). NGC 4106 shows extended LINER-type emission in its disc, as well as its nucleus.

The accurate determination of the metallicity is critically dependent on emission lines sensitive to the electron temperature, which are not detected in the spectra of the objects. Therefore, to estimate the oxygen abundance of the gas phase in the nuclear regions of each galaxy, indirect methods that use relatively strong emission lines easily observed in AGNs or SFs and/or photoionization models should be applied. The most common method for estimating the oxygen abundance uses the $R_{23} = ([\mathrm{O\,II}]\,\lambda3727 + [\mathrm{O\,III}]\,\lambda\lambda4959{,}5007)/\mathrm{H}\beta$ parameter initially proposed by Pagel et al. (1979). We used the R_{23} indicator to estimate the metallicity in the nuclear regions of both galaxies, comparing the observed values with a grid of photoionization models from the CLOUDY code (Ferland et al. 2017).

The grids were built following the same methodology presented in Dors et al. (2014, 2017). We created theoretical models based on power laws of the form $f_\nu \propto \nu^\alpha$, where α was assumed to be equal to $\alpha = -1.4$, which is a representative value for AGNs (Zamorani et al. 1981; Miller et al. 2011), with metallicities of $Z = 0.2, 0.5, 1.0, 2.0, 3.0$ and $4.0\,\mathrm{Z}_\odot$, ionization parameter $\log U = -3.46, -2.46, 1.46, 0.46, 0.54, 1.54$ and 2.54, and fixed electron density value of $500\,\mathrm{cm}^{-3}$. The solar oxygen abundance of $12 + \log(\mathrm{O/H})_\odot = 8.69 \pm 0.05$ is taken from Allende Prieto, Lambert & Asplund (2001).

Fig. 13 shows the R_{23} versus $[\mathrm{O\,III}]/[\mathrm{O\,II}]$ diagram, with the observed values superposed on the computed models. Black and red squares correspond to the nuclear apertures in NGC 4105 and NGC 4106, respectively. The central O/H abundances for each object were obtained by linear interpolation from the model grid, which resulted in $12 + \log(\mathrm{O/H}) = 9.03 \pm 0.02$ and $12 + \log(\mathrm{O/H}) = 8.69 \pm 0.05$ for NGC 4105 and NGC 4106, respectively. We compared the metallicities obtained from the gas and stellar phase and verified that for NGC 4106 the $Z/\mathrm{Z}_\odot$ value is the same, that is, $Z/\mathrm{Z}_\odot = 1$, and for NGC 4105 the metallicity in the stellar phase ($Z/\mathrm{Z}_\odot = 1.6$) is slightly lower than that obtained from the gas phase, $Z/\mathrm{Z}_\odot = 2.2$, by about 30 per cent.

7 CONCLUSIONS

In the present work, we aimed to understand the effects of interaction in the stellar and gas kinematics, stellar populations, and ionized gas properties of the strongly interacting system pair AM 1204−292. Long-slit spectra in the range 3000–7050 Å were obtained with the Goodman High Throughput Spectrograph attached to the 4.1-m SOAR telescope. The main results are the following.

(i) No signs of rotation were detected in the stellar components over both slit directions observed for NGC 4105. As for gas, the kinematics show a clear pattern of rotation for PA = 118°, i.e. gas and stars do not share the same kinematics. We can deduce from this that the ionized gas in NGC 4105 is of external origin and that it must have been incorporated into the galaxy recently. However, it was not the result of the ongoing interaction with NGC 4106, as the modelling of the system dynamics indicates. In contrast, NGC 4106 shows nearly symmetrical rotation curves across both slit directions and a dynamical mass of $1.6 \times 10^{10}\,\mathrm{M}_\odot$ was calculated from $V_0 = 138 \pm 6\,\mathrm{km\,s}^{-1}$ at a radius of 3.64 kpc.

(ii) We also perform a set of *N*-body numerical simulations of the encounter between both components using the P-Gadget3 TREEPM/SPH code. It was found that perigalacticum would have occurred about 14.2 Myr ago. At this point, the system was undergoing an outbreak of star formation. In addition, our models successfully reproduce some important observational features of the system.

(iii) The contribution of the stellar components in relation to the optical flux at λ5870 Å for both galaxies is dominated by the old ($t > 1 \times 10^9$ yr) population, with a non-negligible contribution from an intermediate population and a small amount of young population.

(iv) The electron density estimates for the pair AM 1204−292 are systematically higher than those derived for isolated galaxies in the literature. Some regions of the NGC 4106 and NGC 4105 galaxies show an increment of N_e towards the outskirts and in the close central region, respectively.

(v) We observe a LINER-like line ratio in all regions of NGC 4105, while NGC 4106 shows extended LINER-type emission in the disc, as well as the nuclei.

(vi) The central O/H abundances of NGC 4105 and NGC 4106 were obtained by linear interpolation from a model grid and intensity of emission lines, which resulted in $12 + \log(\mathrm{O/H}) = 9.03 \pm 0.02$ and $12 + \log(\mathrm{O/H}) = 8.69 \pm 0.05$ for NGC 4105 and NGC 4106, respectively.

(vii) We compared the metallicities obtained from the gas and stellar phase and verified that for NGC 4106 $Z/\mathrm{Z}_\odot$ is the same, i.e. $Z/\mathrm{Z}_\odot = 1$, and for NGC 4105 the metallicity in the stellar phase ($Z/\mathrm{Z}_\odot = 1.6$) is slightly lower than that obtained from the gas phase, $Z/\mathrm{Z}_\odot = 2.2$, about 30 per cent.

In summary, the current work has contributed to the understanding of how mutual dynamic perturbation in a strongly interacting galaxy pair can disturb the global morphology of each galaxy, the stellar and gas kinematics, the physical–chemical properties of the gaseous component, and the stellar formation inside each of the galaxies. The AGN phenomenon can also be intensified by encounters between galaxies containing gas in some amount, investigated in this work as well. Curiously, the system contains galaxies of different morphological types (and with distinct masses too), such that one object could have been wrongly classified as a spiral galaxy due to the formation of a double tidal stellar tail during the interaction as proposed by us, which has easily been misinterpreted as a spiral arm. This kind of observational study on a detailed characterization of both stellar and gaseous components, when confronted with a set of

N-body numerical simulations for the encounter, has provided a lot of interesting results about the formation and evolution of interacting galaxies in very low-density environments like nearby galaxy pairs and sparse groups.

ACKNOWLEDGEMENTS

DAR is grateful for the scholarship from CAPES and CNPq foundations for the PCI/MCTIC/INPE postdoc fellowship (process 300082/2016-9). IR and AK thank the Brazilian foundation CNPq/MCTIC (grants number 313489/2018-1 and 311331/2017-3, respectively). AK thanks FAPESP (grant number 2016/21532-9). Numerical simulations were run on the *Hypercubo* HPC cluster at IP&D-UNIVAP (FINEP 01.10.0661-00, FAPESP 2011/13250-0, FAPESP 2013/17247-9 and FAPESP 2014/10489-0). We all acknowledge usage of the HyperLeda database (http://leda.univ-lyon1.fr). This research made use of the NASA/IPAC Extragalactic Database (NED), which is operated by the Jet Propulsion Laboratory, California Institute of Technology, under contract with the National Aeronautics and Space Administration. IRAF is written and supported by the National Optical Astronomy Observatories (NOAO) in Tucson, Arizona. NOAO is operated by the Association of Universities for Research in Astronomy (AURA), Inc. under cooperative agreement with the National Science Foundation. We thank Louis Ho, Zhao-Yu Li, and the CGS team for kindly providing the image in the *I* band of AM 1204−292.

DATA AVAILABILITY

The data underlying this article will be shared on reasonable request to the corresponding author.

REFERENCES

Allende Prieto C., Lambert D. L., Asplund M., 2001, ApJ, 556, L63
Alonso S., Coldwell G., Duplancic F., Mesa V., Lambas D. G., 2018, A&A, 618, A149
Arp H., Madore B., Roberton W., 1987, A Catalogue of Southern Peculiar Galaxies and Associations (Two-Volume Hardback Set). Cambridge Univ. Press, Cambridge
Asari N. V., Cid Fernandes R., Stasińska G., Torres-Papaqui J. P., Mateus A., Sodré L., Schoenell W., Gomes J. M., 2007, MNRAS, 381, 263
Bait O., Barway S., Wadadekar Y., 2017, MNRAS, 471, 2687
Baldwin J. A., Phillips M. M., Terlevich R., 1981, PASP, 93, 5
Barnes J. E., 2002, MNRAS, 333, 481
Barrera-Ballesteros J. K. et al., 2015, A&A, 579, A45
Bertola F., Bettoni D., Danziger J., Sadler E., Sparke L., de Zeeuw T., 1991, ApJ, 373, 369
Binney J., Tremaine S., 2008, Galactic Dynamics, 2nd edn. Princeton Univ. Press, Princeton
Bottinelli L., Gouguenheim L., 1979, A&A, 74, 172
Bresolin F., Ryan-Weber E., Kennicutt R. C., Goddard Q., 2009, ApJ, 695, 580
Bruzual G., Charlot S., 2003, MNRAS, 344, 1000
Calzetti D., Kinney A. L., Storchi-Bergmann T., 1994, ApJ, 429, 582
Caon N., Macchetto D., Pastoriza M., 2000, ApJS, 127, 39
Capaccioli M. et al., 2015, A&A, 581, A10
Capetti A., Baldi R. D., 2011, A&A, 529, A126
Cardelli J. A., Clayton G. C., Mathis J. S., 1989, ApJ, 345, 245
Chabrier G., 2003, PASP, 115, 763
Cid Fernandes R., Gu Q., Melnick J., Terlevich E., Terlevich R., Kunth D., Rodrigues Lacerda R., Joguet B., 2004, MNRAS, 355, 273
Cid Fernandes R., Mateus A., Sodré L., Stasińska G., Gomes J. M., 2005, MNRAS, 358, 363
Cid Fernandes R., Asari N. V., Sodré L., Stasińska G., Mateus A., Torres-Papaqui J. P., Schoenell W., 2007, MNRAS, 375, L16
Croton D. J. et al., 2006, MNRAS, 365, 11
Dalcanton J. J., 2007, ApJ, 658, 941
Darg D. W. et al., 2010, MNRAS, 401, 1552
De Mello D. F., Keel W. C., Sulentic J. W., Rampazzo R., Bica E., White R. E. I., 1995, A&A, 297, 331
De Mello D. F., Sulentic J. W., de Souza R. E., Reduzzi L., Rampazzo R., 1996, A&A, 308, 387
De Vaucouleurs G., de Vaucouleurs A., Corwin Jr. H. G., Buta R. J., Paturel G., Fouque P., 1991, S&T, 82, 621 (RC3)
Di Matteo P., Bournaud F., Martig M., Combes F., Melchior A.-L., Semelin B., 2008, A&A, 492, 31
Diniz M. R., Riffel R. A., Dors O. L., 2018, Res. Notes Amer. Astron. Soc., 2, 3
Donley J. L. et al., 2018, ApJ, 853, 63
Donzelli C. J., Pastoriza M. G., 2000, AJ, 120, 189
Dors O. L., Jr., Arellano-Córdova K. Z., Cardaci M. V., Hägele G. F., 2017, MNRAS, 468, L113
Dors O. L., Cardaci M. V., Hägele G. F., Krabbe Â. C., 2014, MNRAS, 443, 1291
Drzazga R. T., Chyży K. T., Jurusik W., Wiórkiewicz K., 2011, A&A, 533, A22
Duflot M., Fehrenbach C., Mannone C., Burnage R., Genty V., 1995, A&AS, 110, 177
Eliche-Moral M. C., González-García A. C., Balcells M., Aguerri J. A. L., Gallego J., Zamorano J., Prieto M., 2011, A&A, 533, A104
Ellison S. L., Patton D. R., Mendel J. T., Scudder J. M., 2011, MNRAS, 418, 2043
Ferland G. J. et al., 2017, Rev. Mex. Astron. Astrofis., 53, 385
Fernandes de Mello D., 1995, PASP, 107, 1129
Focardi P., Zitelli V., Marinoni S., 2008, A&A, 484, 655
González Delgado R. M. et al., 2015, A&A, 581, A103
Goudfrooij P., Hansen L., Jorgensen H. E., Norgaard-Nielsen H. U., 1994, A&AS, 105, 341
Grützbauch R., Trinchieri G., Rampazzo R., Held E. V., Rizzi L., Sulentic J. W., Zeilinger W. W., 2007, AJ, 133, 220
Grützbauch R., Zeilinger W. W., Rampazzo R., Held E. V., Sulentic J. W., Trinchieri G., 2009, A&A, 502, 473
Heckman T. M., 1980, A&A, 500, 187
Henriques B. M. B., White S. D. M., Lilly S. J., Bell E. F., Bluck A. F. L., Terrazas B. A., 2019, MNRAS, 485, 3446
Hernquist L., 1990, ApJ, 356, 359
Herrera-Endoqui M., Díaz-García S., Laurikainen E., Salo H., 2015, A&A, 582, A86
Ho L. C., Filippenko A. V., Sargent W. L. W., 1997, ApJS, 112, 315
Ho L. C., Li Z.-Y., Barth A. J., Seigar M. S., Peng C. Y., 2011, ApJS, 197, 21
Huang S., Ho L. C., Peng C. Y., Li Z.-Y., Barth A. J., 2016, ApJ, 821, 114
Kauffmann G. et al., 2003, MNRAS, 346, 1055
Kewley L. J., Dopita M. A., Sutherland R. S., Heisler C. A., Trevena J., 2001, ApJ, 556, 121
Kewley L. J., Rupke D., Zahid H. J., Geller M. J., Barton E. J., 2010, ApJ, 721, L48
Kim T. et al., 2012, ApJ, 753, 43
Knapen J. H., Cisternas M., Querejeta M., 2015, MNRAS, 454, 1742
Kobayashi C., 2004, MNRAS, 347, 740
Koprolin W., Zeilinger W. W., 2000, A&AS, 145, 71
Krabbe A. C., Pastoriza M. G., Winge C., Rodrigues I., Ferreiro D. L., 2008, MNRAS, 389, 1593
Krabbe A. C., Pastoriza M. G., Winge C., Rodrigues I., Dors O. L., Ferreiro D. L., 2011, MNRAS, 416, 38
Krabbe A. C., Rosa D. A., Dors O. L., Pastoriza M. G., Winge C., Hägele G. F., Cardaci M. V., Rodrigues I., 2014, MNRAS, 437, 1155
Kurtz M. J., Mink D. J., 1998, PASP, 110, 934
Larson R. B., Tinsley B. M., 1978, ApJ, 219, 46
Li Z.-Y., Ho L. C., Barth A. J., Peng C. Y., 2011, ApJS, 197, 22
Longhetti M., Rampazzo R., Bressan A., Chiosi C., 1998, A&AS, 130, 267
Longhetti M., Bressan A., Chiosi C., Rampazzo R., 2000, A&A, 353, 917

Macchetto F., Pastoriza M., Caon N., Sparks W. B., Giavalisco M., Bender R., Capaccioli M., 1996, A&AS, 120, 463
Makarov D., Prugniel P., Terekhova N., Courtois H., Vauglin I., 2014, A&A, 570, A13
Mateus A., Sodré L., Cid Fernandes R., Stasińska G., Schoenell W., Gomes J. M., 2006, MNRAS, 370, 721
Mauch T., Sadler E. M., 2007, MNRAS, 375, 931
Mendes de Oliveira C., Hickson P., 1994, ApJ, 427, 684
Méndez-Abreu J., Sánchez-Janssen R., Aguerri J. A. L., Corsini E. M., Zarattini S., 2012, ApJ, 761, L6
Miller B. P., Brandt W. N., Schneider D. P., Gibson R. R., Steffen A. T., Wu J., 2011, ApJ, 726, 20
Mink D. J., Wyatt W. F., 1995, in Shaw R. A., Payne H. E., Hayes J. J. E., eds, ASP Conf. Ser. Vol. 77, Astronomical Data Analysis Software and Systems IV. Astron. Soc. Pac., San Francisco, p. 496
Mora M. D., Torres-Flores S., Firpo V., Hernandez-Jimenez J. A., Urrutia-Viscarra F., Mendes de Oliveira C., 2019, MNRAS, 488, 830
Moreno J., Torrey P., Ellison S. L., Patton D. R., Bluck A. F. L., Bansal G., Hernquist L., 2015, MNRAS, 448, 1107
Muñoz-Elgueta N., Torres-Flores S., Amram P., Hernandez-Jimenez J. A., Urrutia-Viscarra F., Mendes de Oliveira C., Gómez-López J. A., 2018, MNRAS, 480, 3257
Obreja A., Domínguez-Tenreiro R., Brook C., Martínez-Serrano F. J., Doménech-Moral M., Serna A., Mollá M., Stinson G., 2013, ApJ, 763, 26
Oser L., Ostriker J. P., Naab T., Johansson P. H., Burkert A., 2010, ApJ, 725, 2312
Pagel B. E. J., Edmunds M. G., Blackwell D. E., Chun M. S., Smith G., 1979, MNRAS, 189, 95
Patton D. R., Ellison S. L., Simard L., McConnachie A. W., Mendel J. T., 2011, MNRAS, 412, 591
Patton D. R., Torrey P., Ellison S. L., Mendel J. T., Scudder J. M., 2013, MNRAS, 433, L59
Pengelly R. M., 1964, MNRAS, 127, 145
Phillips M. M., Jenkins C. R., Dopita M. A., Sadler E. M., Binette L., 1986, AJ, 91, 1062
Presotto V., Iovino A., Pompei E., Temporin S., 2010, A&A, 510, A31
Reduzzi L., Rampazzo R., 1996, A&AS, 116, 515
Renaud F., 2010, PhD thesis, Observatoire Astronomique, Strasbourg
Roche N., Humphrey A., Gomes J. M., Papaderos P., Lagos P., Sánchez S. F., 2015, MNRAS, 453, 2349
Rodrigues I., Dottori H., Brinks E., Mirabel I. F., 1999, AJ, 117, 2695
Rogers B., Ferreras I., Kaviraj S., Pasquali A., Sarzi M., 2009, MNRAS, 399, 2172
Rosa D. A., Dors O. L., Krabbe A. C., Hägele G. F., Cardaci M. V., Pastoriza M. G., Rodrigues I., Winge C., 2014, MNRAS, 444, 2005
Rosa D. A., Milone A. C., Krabbe A. C., Rodrigues I., 2018, Ap&SS, 363, 131
Salo H. et al., 2015, ApJS, 219, 4
Samurović S., Danziger I. J., 2005, MNRAS, 363, 769
Sánchez S. F. et al., 2012, A&A, 538, A8
Sánchez S. F. et al., 2013, A&A, 554, A58
Sánchez S. F. et al., 2014, A&A, 563, A49
Sandage A., Tammann G. A., 1981, A Revised Shapley-Ames Catalog of Bright Galaxies. Carnegie Institution of Washington, Publ. 635
Satyapal S., Ellison S. L., McAlpine W., Hickox R. C., Patton D. R., Mendel J. T., 2014, MNRAS, 441, 1297
Silverman J. D. et al., 2011, ApJ, 743, 2
Springel V., 2005, MNRAS, 364, 1105
Springel V., Hernquist L., 2002, MNRAS, 333, 649
Springel V., Hernquist L., 2003, MNRAS, 339, 289
Tonry J., Davis M., 1979, AJ, 84, 1511
Toomre A., Toomre J., 1972, ApJ, 178, 623
Torrey P., Cox T. J., Kewley L., Hernquist L., 2012, ApJ, 746, 108
Trinchieri G., Rampazzo R., 2001, A&A, 374, 454
Trouille L., Barger A. J., Tremonti C., 2011, ApJ, 742, 46
Véron-Cetty M.-P., Véron P., 2010, A&A, 518, A10
Weaver J. et al., 2018, A&A, 614, A32
Woods D. F., Geller M. J., 2007, AJ, 134, 527
Wright E. L., 2006, PASP, 118, 1711
Xu C. K. et al., 2010, ApJ, 713, 330
Yadav J. K., Chen X., 2018, JA&A, 39, 31
Yan R., Newman J. A., Faber S. M., Konidaris N., Koo D., Davis M., 2006, ApJ, 648, 281
Zamorani G. et al., 1981, ApJ, 245, 357
Zibetti S., Gallazzi A. R., Hirschmann M., Consolandi G., Falcón-Barroso J., van de Ven G., Lyubenova M., 2020, MNRAS, 491, 3562

This paper has been typeset from a TEX/LATEX file prepared by the author.